Optics and Lasers in Engineering 161 (2023) 107327

Contents lists available at ScienceDirect

Optics and Lasers in Engineering

journal homepage: www.elsevier.com/locate/optlaseng

Two-step phase-shifting algorithms with background removal and no background removal

Yu Zhang [a,b,*], Bao Liu [a], Rongguang Liang [c]

[a] Institute of Materials Physics, College of Science, Northeast Electric Power University, Jilin, Jilin 132012, China
[b] State Key Laboratory of Applied Optics, Changchun Institute of Optics, Fine Mechanics and Physics, Chinese Academy of Sciences, Changchun, Jilin 130022, China
[c] James C. Wyant College of Optical Sciences, University of Arizona, Tucson, AZ 85721, USA

ARTICLE INFO

Keywords:
Two-step phase-shifting algorithm
Background removal
Phase shift
Accuracy

ABSTRACT

To balance the accuracy and speed of phase reconstruction, two-step phase-shifting algorithms (TS-PSAs) have been developed. TS-PSAs can be divided into two types, one is TS-PSAs with background removal (TS-PSAs-BR), and the other is TS-PSAs with no background removal (TS-PSAs-NBR). We select 6 well-reputed TS-PSAs-BR and 4 TS-PSAs-NBR proposed by the authors of this paper for performance comparison. In order to remove the background, the Hilbert-Huang Transform (HHT) and mean intensity subtraction are used respectively. We compare 10 TS-PSAs with different fringe types, different levels of noise, different phase shifts, different fringe numbers and computational time in the simulations, and the experiments are also performed to compare them. Finally, we rank TS-PSAs according to their comparative results, and Euclidean matrix norm of sum and difference map and fast least-squares algorithm (EMNSD&FLSA) provides the best overall performance, it can achieve high accuracy and high efficiency.

1. Introduction

The level of optical metrology determines the level of optical manufacturing technology, and the phase-shifting interferometry (PSI) as an easy, high-speed and accurate optical testing tool is usually used during or after optical fabrication [1–5]. Both accuracy and efficiency are important to PSI. Outstanding phase-shifting algorithms (PSAs) can reduce the requirements on the interferometer hardware and environment, and further improve the accuracy and speed of PSI.

Traditional PSAs with known phase shifts (such as the three-step algorithm, Carré algorithm, the family of averaging algorithms, Hariharan algorithm, etc.) are easily affected by the miscalibration of piezo-transducer and environmental errors [6]. In order to save time, many single-step PSAs were developed [7–12]. Nevertheless, the sign of phase is difficult to judge by only one interferogram, this may be the main reason impeding the development of this kind of PSA. Although many PSAs have solved this problem, their cost is more computational time, which violates the original intention of fast phase reconstruction. In some high-precision events, accurate phase reconstruction is of interest. Hence, many scientists researched the multi-step PSAs with more than three interferograms, such as the advanced iterative algorithm (AIA) [13], principal component analysis method (PCA) [14–18], advanced Gram-Schmidt orthonormalization algorithm (GS3) [19], Euclidean distance method (ED) [20], Euclidean matrix norm algorithm (EMN) [21], VU factorization method (VU) [22], volume enclosed by a surface method (VES) [23–25], etc. However, all of them have different limitations, it's difficult to reconstruct the phase with high accuracy and efficiency simultaneously. Comparatively, two-step random PSAs can avoid the effect of phase shift error, solve the sign ambiguity problem of the single-step PSAs, and balance the accuracy and speed [26–52].

Whereas two-step PSAs (TS-PSAs) also face the challenge, the number of unknowns is more than the number of interferograms. One way to reduce the number of unknowns is to remove the background. Many TS-PSAs with background removal (TS-PSAs-BR) have been developed. In [29], the authors reported a two-step Gram-Schmidt orthonormalization method (GS) which can calculate the phase directly using two interferograms without the phase shift estimation, it's fast and easy to perform, so it's widely used in two-step PSI. In [30], a TS-PSA was proposed to determine the phase shift by the ratio of extreme values of the interference (EVI). When the interferograms are of poor quality, EVI may perform poorly. A simple method to calculate the phase shift and phase using orthogonality of diamond diagonal vectors (DDV) was proposed [34]. In this approach, there are so many approximations that the accuracy is affected. A straightforward and fast two-step PSA was proposed, which obtains the phase shift by calculating the quotient of inner products of phase-shifting interferograms (QIP), but its accuracy is not very high due to the approximation in inner products calculation [35]. In [44], the authors obtained the phase shift by solving a quartic poly-

* Corresponding author at: Institute of Materials Physics, College of Science, Northeast Electric Power University, Jilin 132012, China.
E-mail address: 20122412@neepu.edu.cn (Y. Zhang).

https://doi.org/10.1016/j.optlaseng.2022.107327
Received 8 July 2022; Received in revised form 7 September 2022; Accepted 3 October 2022
Available online 18 October 2022

nomial equation (QPE). Although the cosine of phase shift can be easily extracted by [35] and [44], the range of phase shift is limited between 0 to π. In [45], the authors proposed a random TS-PSA to reconstruct the phase using the phase shift corresponding to the minimum coefficient of variation (CVM) of the modulation amplitude.

Background removal methods can be divided into 2 types. One is the filtering algorithm that only filters the background, such as Gaussian high-pass filtering [30,34,35,45], mean intensity subtraction [31,53], etc. The other is the filtering algorithm that simultaneously filters background and noise, such as Hilbert-Huang Transform (HHT) [32,45,46,54,55] and some fringe pattern normalization methods [56,57]. In general, the first type costs less time, but the noise will affect the accuracy of phase reconstruction. Although the second type can filter the noise, it takes more time, and the filtering error will also affect the accuracy. Different background removal methods have different effects on phase reconstruction, hence we will evaluate TS-PSAs-BR with different background removal methods.

To avoid errors in the background removal process, some TS-PSAs with no background removal (TS-PSAs-NBR) have been researched. These TS-PSAs-NBR can be divided into two types. One is based on Lissajous ellipse fitting method (LEF) [47], the authors of this paper designed two TS-PSAs-NBR based on LEF, GS or PCA without any background removal is firstly performed, and then phase extraction is performed using LEF, which doesn't require an iterative process, but LEF takes a certain amount of time [48,49]. The other is based on least-squares algorithm (LSA), the authors of this paper proposed a Euclidean matrix norm of sum and difference map and fast least-squares algorithm (EMNSD&FLSA) [50]. EMNSD is firstly used to calculate the initial phase, and then limited pixels are selected to participate LSA to obtain accurate phase shift, finally, the final phase is reconstructed using the whole pixels, EMNSD&FLSA is accurate and time-saving. Sometimes LEF and LSA can be combined, such as Lissajous ellipse fitting and least-squares iterative technologies (LEF&LSI) [51]. LEF is firstly used to calculate the iterative initial value, and then LSI is used to calculate the more accurate phase. The greatest advantage of LEF&LSI is that it can obtain the background intensity and modulation amplitude of each interferogram, therefore, it has high accuracy. However, it takes a lot of time since all pixels are taken part in LSI, and LEF also takes a certain amount of time.

In this paper, we will review the recent well-reputed and widely-used TS-PSAs. In Section 2, the expressions of two phase-shifting interferograms will be introduced. Then, we will thoroughly explain two types of TS-PSAs—TS-PSAs-BR and TS-PSAs-NBR in Section 3. TS-PSAs-BR include GS, DDV, EVI, QIP, CVM and QPE, and TS-PSAs-NBR include GS&LEF, PCA&LEF, LEF&LSI and EMNSD&FLSA. In Section 4, the performance of 10 TS-PSAs will be evaluated and compared by simulations with different levels of noise, different types of fringes, different phase shifts, different fringe numbers and computational time. Moreover, both noise and filtering error will affect the performance of TS-PSAs-BR, so which one has more effect on the phase reconstruction is worth studying. Gaussian high-pass filtering, mean intensity subtraction and HHT are widely used in background removal, hence they will be respectively used for performance comparison before performing TS-PSAs-BR. In Section 5, the experiments with different types of fringes will be performed to further compare 10 TS-PSAs. Finally, TS-PSAs will be ranked, and the applicable situations of different TS-PSAs will be given according to the simulation and experimental analysis. In addition, the improvement direction of TS-PSAs will be given.

2. Expressions of two phase-shifting interferograms

Eqs. (1) and (2) represent the intensity of two phase-shifting interferograms.

$$I_1(x,y) = a(x,y) + b(x,y)\cos(\varphi(x,y)) \tag{1}$$

$$I_2(x,y) = a(x,y) + b(x,y)\cos(\varphi(x,y) + \delta) \tag{2}$$

where $a(x,y)$and $b(x,y)$are the background intensity and modulation amplitude, $\varphi(x,y)$and δrepresent the measured phase and unknown phase shift. The position (x,y) is omitted to simplify the following expressions.

3. Two-step phase-shifting algorithms (TS-PSAs)

3.1. TS-PSAs with background removal (TS-PSAs-BR)

3.1.1. Gram-Schmidt orthonormalization method (GS)

GS was proposed by Vargas et al. $\tilde{I}_1$ and $\tilde{I}_2$ are the interferograms with background removed.

Firstly, $\tilde{I}_1$is normalized as

$$\hat{I}_1 = b\cos(\varphi)/\sqrt{\sum_{x=1}^{N_x}\sum_{y=1}^{N_y}(b\cos(\varphi))^2} \tag{3}$$

Then, orthogonalizing $\widehat{I}_2$ with respect to $\tilde{I}_1$, subtracting its projection as

$$\widehat{I}_2 = -b\sin(\varphi)\sin(\delta) \tag{4}$$

Finally, obtaining $\hat{I}_2$by dividing $\widehat{I}_2$ by its norm.

$$\hat{I}_2 = -b\sin(\varphi)/\sqrt{\sum_{x=1}^{N_x}\sum_{y=1}^{N_y}(b\sin(\varphi))^2} \tag{5}$$

If there is more than one fringe in the interferograms,

$$\sqrt{\sum_{x=1}^{N_x}\sum_{y=1}^{N_y}(b\cos(\varphi))^2} \approx \sqrt{\sum_{x=1}^{N_x}\sum_{y=1}^{N_y}(b\sin(\varphi))^2} \tag{6}$$

The phase can be directly obtained by

$$\varphi = \arctan\left(-\hat{I}_2/\hat{I}_1\right) \tag{7}$$

3.1.2. Diamond diagonal vectors algorithm (DDV)

DDV was proposed by Deng et al. Given the interferograms after removing the background as $\tilde{I}_1$ and $\tilde{I}_2$, their length can be calculated by

$$\|\tilde{I}_1\| = \sqrt{\sum_{x=1}^{N_x}\sum_{y=1}^{N_y} b^2\cos^2(\varphi)} \tag{8}$$

$$\|\tilde{I}_2\| = \sqrt{\sum_{x=1}^{N_x}\sum_{y=1}^{N_y} b^2\cos^2(\varphi+\delta)} \tag{9}$$

If there is more than one fringe in the interferograms,

$$\|\tilde{I}_1\| \approx \|\tilde{I}_2\| \tag{10}$$

It means that $\tilde{I}_1$ and $\tilde{I}_2$have the same length but go in different directions. According to the parallelogram rule, the sum and the difference of $\tilde{I}_1$ and $\tilde{I}_2$ are perpendicular. Therefore, two perpendicular diamond diagonal vectors are expressed as

$$\tilde{I}_{dif} = \tilde{I}_1 - \tilde{I}_2 \tag{11}$$

$$\tilde{I}_{sum} = \tilde{I}_1 + \tilde{I}_2 \tag{12}$$

When the fringe number is more than one,

$$\frac{\delta}{2} \approx \arctan\left(\frac{\|\tilde{I}_{dif}\|}{\|\tilde{I}_{sum}\|}\right) \tag{13}$$

After the phase shift calculation, the phase can be obtained by

$$\varphi = \arctan\left(\frac{\tilde{I}_{dif}\|\tilde{I}_{sum}\|}{\tilde{I}_{sum}\|\tilde{I}_{dif}\|}\right) - \frac{\delta}{2} \tag{14}$$

3.1.3. Extreme values of the interference algorithm (EVI)

EVI was designed by Deng et al. With the interferograms after background removal, the phase shift can be obtained by

$$\delta=\frac{\sum_{i=1}^{P}\arccos\left(\frac{\tilde{I}_{2,p_i}}{\tilde{I}_{1,p_i}}\right)+\sum_{j=1}^{V}\arccos\left(\frac{\tilde{I}_{2,v_j}}{\tilde{I}_{1,v_j}}\right)}{P+V} \tag{15}$$

Where P and V are respectively the number of maximum and minimum intensity in $\tilde{I}_1$, and $p_i(i=1,2,\cdots P)$ and $v_j(j=1,2,\cdots V)$ are the corresponding pixel positions of maximum and minimum intensity.

After the phase shift calculation, the phase can be directly obtained by

$$\varphi=\arctan\left(\frac{\tilde{I}_1\cos(\delta)-\tilde{I}_2}{\tilde{I}_1\sin(\delta)}\right) \tag{16}$$

3.1.4. Quotient of inner products algorithm (QIP)

QIP was proposed by Niu et al. The inner products of $\tilde{I}_1$ and $\tilde{I}_1$can be expressed by

$$s_1=\left\langle\tilde{I}_1,\tilde{I}_1\right\rangle=\sum_{x=1}^{M}\sum_{y=1}^{N}\left[b^2\cos^2(\varphi)\right] \tag{17}$$

And the inner products of $\tilde{I}_1$ and $\tilde{I}_2$ can be calculated by

$$s_2=\left\langle\tilde{I}_1,\tilde{I}_2\right\rangle\approx\sum_{x=1}^{M}\sum_{y=1}^{N}\left[b^2\cos^2(\varphi)\right]\cos(\delta) \tag{18}$$

Next, the phase shift can be determined by

$$\delta=\arccos\left(s_2/s_1\right)=\arccos\left(\frac{\left\langle\tilde{I}_1,\tilde{I}_2\right\rangle}{\left\langle\tilde{I}_1,\tilde{I}_1\right\rangle}\right) \tag{19}$$

At last, the phase can be reconstructed by Eq. (16).

3.1.5. Coefficient of variation minimization method (CVM)

Cheng et al. proposed a TS-PSA based on CVM. The modulation amplitude $b$can be expressed as a function of the phase shift δ,

$$b=\sqrt{\tilde{I}_1^2+\left[\tilde{I}_1/\tan(\delta)-\tilde{I}_2/\sin(\delta)\right]^2} \tag{20}$$

The coefficient of variation (CV) of $b$can be defined as

$$C_V(b)=std(b)/mean(b) \tag{21}$$

where $std(\cdot)$represents the standard deviation, and $mean(\cdot)$represents the mean.

The accurate phase shift δ is at the position where $C_V$is minimum,

$$\delta=\arg\min_{\delta}\ C_V(b) \tag{22}$$

The classical Fibonacci search algorithm is used to search the phase shift, and then the corresponding phase is reconstructed by Eq. (16).

3.1.6. Quartic polynomial equation solving algorithm (QPE)

Cheng et al. proposed a fast and accurate TS-PSA based on the quartic polynomial equation solution.

If the fringe number is more than one, the phase shift can be estimated by

$$\begin{aligned}\delta=\operatorname{argmin}\Bigg\{&\left(A\frac{\cos(\delta)}{\sin(\delta)}-C\frac{1}{\sin(\delta)}\right)^2\\&+\left(A-A\frac{1}{\tan^2(\delta)}-B\frac{1}{\sin^2(\delta)}+2C\frac{\cos(\delta)}{\sin^2\delta}\right)^2\Bigg\}\end{aligned} \tag{23}$$

where $A=\sum_{x=1}^{N_x}\sum_{y=1}^{N_y}\tilde{I}_1^2$, $B=\sum_{x=1}^{N_x}\sum_{y=1}^{N_y}\tilde{I}_2^2$, $A=\sum_{x=1}^{N_x}\sum_{y=1}^{N_y}\tilde{I}_1\tilde{I}_2$.

After setting the derivative of the target function to zero, the optimal $\cos(\delta)$will be ultimately found by the following quartic polynomial equation.

$$\begin{aligned}&3ACz^4-\left(4AB+3C^2+3A^2\right)z^3+(6BC+6AC)z^2\\&-\left(5C^2+2B^2-A^2\right)z+2BC-AC=0\end{aligned} \tag{24}$$

Eq. (24) may have many solutions, and the real solution is closest to C/A. After getting the phase shift, the phase can be obtained by Eq. (16).

3.2. TS-PSAs with no background removal (TS-PSAs-NBR)

3.2.1. Gram-Schmidt orthonormalization and Lissajous ellipse fitting method (GS&LEF)

Traditional GS uses the interferograms with background removed to reconstruct the phase. In order to avoid the extra error caused by background removal, a TS-PSA based on GS&LEF was proposed by the authors of this paper.

Firstly, the interferograms I_1 and I_2 are orthonormalized by GS. The details are in the following.

$$I_1'=I_1/\|I_1\| \tag{25}$$

$$\breve{I}_2=I_2-\left\langle I_2,I_1'\right\rangle\cdot I_1' \tag{26}$$

$$I_2'=\breve{I}_2/\left\|\breve{I}_2\right\| \tag{27}$$

Then, set $D^*=I_1'$ and $N^*=-I_2'$, the ellipse equation is obtained.

$$\left(AN^*+BD^*+C\right)^2+\left(DD^*+E\right)^2=1 \tag{28}$$

In order to calculate the ellipse parameters, including semi-major amplitude a_x, semi-minor amplitude a_y, center offset x_0, y_0 and ellipse orientation angle θ, the coefficients of the ellipse function should be calculated by the Lissajous ellipse fitting method (LEF) firstly.

Finally, Eq. (29) is used to convert the ellipse into a perfect circle centered at the origin.

$$\begin{bmatrix}N_c\\D_c\end{bmatrix}=T*\begin{bmatrix}N^*-x_0\\D^*-y_0\end{bmatrix} \tag{29}$$

where $N_c$and $D_c$are the numerator and denominator of $\tan(\varphi)$after using LEF, the transformation matrix is

$$T=\begin{bmatrix}\cos(-\theta')&-\sin(-\theta')\\\sin(-\theta')&\cos(-\theta')\end{bmatrix}*\begin{bmatrix}1&0\\0&r\end{bmatrix}*\begin{bmatrix}\cos\theta'&-\sin\theta'\\\sin\theta'&\cos\theta'\end{bmatrix} \tag{30}$$

where $\theta'=-\theta$,$r=a_x/a_y$.

At last, the real phase can be calculated by

$$\varphi=\arctan\left(\frac{N_c}{D_c}\right) \tag{31}$$

3.2.2. Principal component analysis and Lissajous ellipse fitting method (PCA&LEF)

A TS-PSA based on PCA&LEF was also proposed by the authors of this paper, it can remove the limit that PCA needs more than three interferograms with uniform phase shift distribution. This TS-PSA requires only two interferograms without background removal, and the phase shift can be set randomly.

Firstly, the size of phase-shifting interferograms is reshaped from $N_x\times N_y$ to $N_xN_y\times 1$, and the intensity of n^{th} phase-shifting interferograms after reshaping is set as the n^{th} column of the matrix I. The covariance matrix C is calculated by

$$C=I^TI \tag{32}$$

Then, the orthogonal matrix $\hat{\Gamma}$ is calculated, and the first and second principal components (z_1 and z_2) which correspond to the highest eigenvalues by $z_i=I\hat{\Gamma}^T$can be obtained.

Take z_2 as the x coordinate and z_1 as the y coordinate to plot an approximate ellipse, then a_x, a_y, x_0 andy_0 of the ellipse can be calculated by LEF.

Finally, the phase is calculated using Eq. (33).

$$\varphi = \tan^{-1}\left(\frac{X - x_0}{Y - y_0} \cdot \frac{a_y}{a_x}\right) - \tan^{-1}\left(\frac{a_x}{a_y}\right) \tag{33}$$

3.2.3. Lissajous ellipse fitting and least-squares iterative algorithm (LEF&LSI)

In order to improve the accuracy of TS-PSAs, the authors of this paper proposed a TS-PSA based on LEF&LSI. The sum and difference of interferograms are calculated by

$$I_{dif} = I_1 - I_2 = 2b\sin\left(\varphi + \frac{\delta}{2}\right)\sin\left(\frac{\delta}{2}\right) \tag{34}$$

$$I_{sum} = I_1 + I_2 = 2a + 2b\cos\left(\varphi + \frac{\delta}{2}\right)\cos\left(\frac{\delta}{2}\right) \tag{35}$$

Then an ellipse equation can be obtained by

$$\left(\frac{I_{dif} - x_0}{a_x}\right)^2 + \left(\frac{I_{sum} - y_0}{a_y}\right)^2 = 1 \tag{36}$$

After LEF, the phase shift and phase can be calculated by

$$\delta = 2\tan^{-1}\left(\frac{a_x}{a_y}\right) \tag{37}$$

$$\varphi = \tan^{-1}\left(\frac{I_{dif} - x_0}{I_{sum} - y_0} \cdot \frac{a_y}{a_x}\right) - \tan^{-1}\left(\frac{a_x}{a_y}\right) \tag{38}$$

Then the phase calculated by Eq. (38) is used as the initial value, and the iteration is performed to improve the accuracy of phase retrieval.

According to the known phase, the absolute phase shift of every interferogram can be determined by

$$\delta_i = \tan^{-1}\left(-\frac{C_i}{B_i}\right) \tag{39}$$

where B_i and C_i can be obtained by

$$\begin{bmatrix} A_i \\ B_i \\ C_i \end{bmatrix} = \begin{bmatrix} N_x \times N_y & \sum_{j=1}^{N_x \times N_y} \cos\varphi_j & \sum_{j=1}^{N_x \times N_y} \sin\varphi_j \\ \sum_{j=1}^{N_x \times N_y} \cos\varphi_j & \sum_{j=1}^{N_x \times N_y} \cos^2\varphi_j & \sum_{j=1}^{N_x \times N_y} \sin\varphi_j \cos\varphi_j \\ \sum_{j=1}^{N_x \times N_y} \sin\varphi_j & \sum_{j=1}^{N_x \times N_y} \sin\varphi_j \cos\varphi_j & \sum_{j=1}^{N_x \times N_y} \sin^2\varphi_j \end{bmatrix}^{-1} \begin{bmatrix} \sum_{j=1}^{N_x \times N_y} I_{i,j} \\ \sum_{j=1}^{N_x \times N_y} I_{i,j}\cos\varphi_j \\ \sum_{j=1}^{N_x \times N_y} I_{i,j}\sin\varphi_j \end{bmatrix} \tag{40}$$

where $i = 1, 2$presents the interferogram index, and $j = 1, 2, \ldots N_x \times N_y$ denotes the pixel position.

Next, the background intensity and modulation amplitude of every phase-shifting interferogram can be obtained as $a_i = A_i$, $b_i = \sqrt{B_i^2 + C_i^2}$, and the relative phase shift can be calculated by $\delta = \delta_2 - \delta_1$. Then Eq. (41) is used to calculate the iterative phase.

$$\varphi = \tan^{-1}\left(\frac{\left(b_2 I_1 \cos(\delta) - b_1 I_2\right) - \left(b_2 a_1 \cos(\delta) - b_1 a_2\right)}{\left(I_1 - a_1\right) b_2 \sin(\delta)}\right). \tag{41}$$

Repeat the iteration until $RMS(\varphi^k - \varphi^{k-1}) < \xi$, the accurate phase and phase shift δ can be gained.

3.2.4. Euclidean matrix norm of sum and difference map and fast least-squares algorithm (EMNSD&FLSA)

To meet the requirements of high-speed optical measurement, EMNSD&FLSA was designed by the authors of this paper.

The sum and difference of the interferograms can be defined as I_{sum} and I_{dif}, the sum without the background can be obtained by

$$\tilde{I}_{sum} \approx I_{sum} - mean\left(I_{sum}\right) \tag{42}$$

Then initial phase can be obtained by

$$\Phi = \varphi + \frac{\delta}{2} = tan^{-1}\left(\frac{\left\|\tilde{I}_{sum}\right\|}{\left\|I_{dif}\right\|} \cdot \frac{I_{dif}}{\tilde{I}_{sum}}\right) \tag{43}$$

For the purpose of saving time, a limited number of Φ, I_1 and I_2at regular intervals are selected. According to the least-squares theory,

$$\begin{bmatrix} a_1 \\ \eta_1 \\ \xi_1 \end{bmatrix} = \begin{bmatrix} N_x \times N_y & \sum_{j=1}^{N_x \times N_y} \cos\left(\Phi_j\right) & \sum_{j=1}^{N_x \times N_y} \sin\left(\Phi_j\right) \\ \sum_{j=1}^{N_x \times N_y} \cos\left(\Phi_j\right) & \sum_{j=1}^{N_x \times N_y} \cos^2\left(\Phi_j\right) & \sum_{j=1}^{N_x \times N_y} \sin\left(\Phi_j\right)\cos\left(\Phi_j\right) \\ \sum_{j=1}^{N_x \times N_y} \sin\left(\Phi_j\right) & \sum_{j=1}^{N_x \times N_y} \sin\left(\Phi_j\right)\cos\left(\Phi_j\right) & \sum_{j=1}^{N_x \times N_y} \sin^2\left(\Phi_j\right) \end{bmatrix}^{-1} \begin{bmatrix} \sum_{j=1}^{N_x \times N_y} I_{1j} \\ \sum_{j=1}^{N_x \times N_y} I_{1j}\cos\left(\Phi_j\right) \\ \sum_{j=1}^{N_x \times N_y} I_{1j}\sin\left(\Phi_j\right) \end{bmatrix} \tag{44}$$

Then, $\frac{\delta}{2}$ can be calculated by

$$\frac{\delta}{2} = \tan^{-1}\left(\frac{\xi_1}{\eta_1}\right) \tag{45}$$

And the background intensity a_1 can also be obtained.

a_2 can be calculated in the same way as above, and $\frac{\delta}{2}$can be obtained again, the average of twice-acquired $\frac{\delta}{2}$ is set as the final $\frac{\delta}{2}$.

The new phase can be calculated by

$$\Phi = \varphi + \delta/2 = \tan^{-1}\left(\cot\left(\frac{\delta}{2}\right) \cdot \frac{I_{dif} - \left(a_1 - a_2\right)}{I_{sum} - \left(a_1 + a_2\right)}\right) \tag{46}$$

Repeat the above iterative process until $RMS(\Phi^l - \Phi^{l-1}) < \varepsilon$, the accurate $\frac{\delta}{2}$ can be obtained by partial pixels.

Finally, the whole pixels of I_{sum} and I_{dif} are used to calculate the final phase as

$$\varphi = \tan^{-1}\left(\cot\left(\frac{\delta}{2}\right) \cdot \frac{I_{dif} - \left(a_1 - a_2\right)}{I_{sum} - \left(a_1 + a_2\right)}\right) - \delta/2 \tag{47}$$

3. Comparisons of TS-PSAs in the simulations

In order to evaluate the performance of TS-PSAs described above, we perform lots of simulations. In the following, all computations are performed with the CPU of Intel(R) Core(TM) i5-8265U and the 8 GB memory, and we use the Matlab software for coding.

We simulate different phase distributions. The phase distributions of Fig. 1(a)-1(d) are set as $\varphi = 5\pi(x^2 + y^2)$, $\varphi = 0.8\pi(x^2 + y^2)$, $\varphi = 5\pi x$ and $\varphi = 4\pi(x^2 + y^2 + x^3 + y^3) + 4[3(1-x)^2 e^{-x^2-(y+1)^2} -$

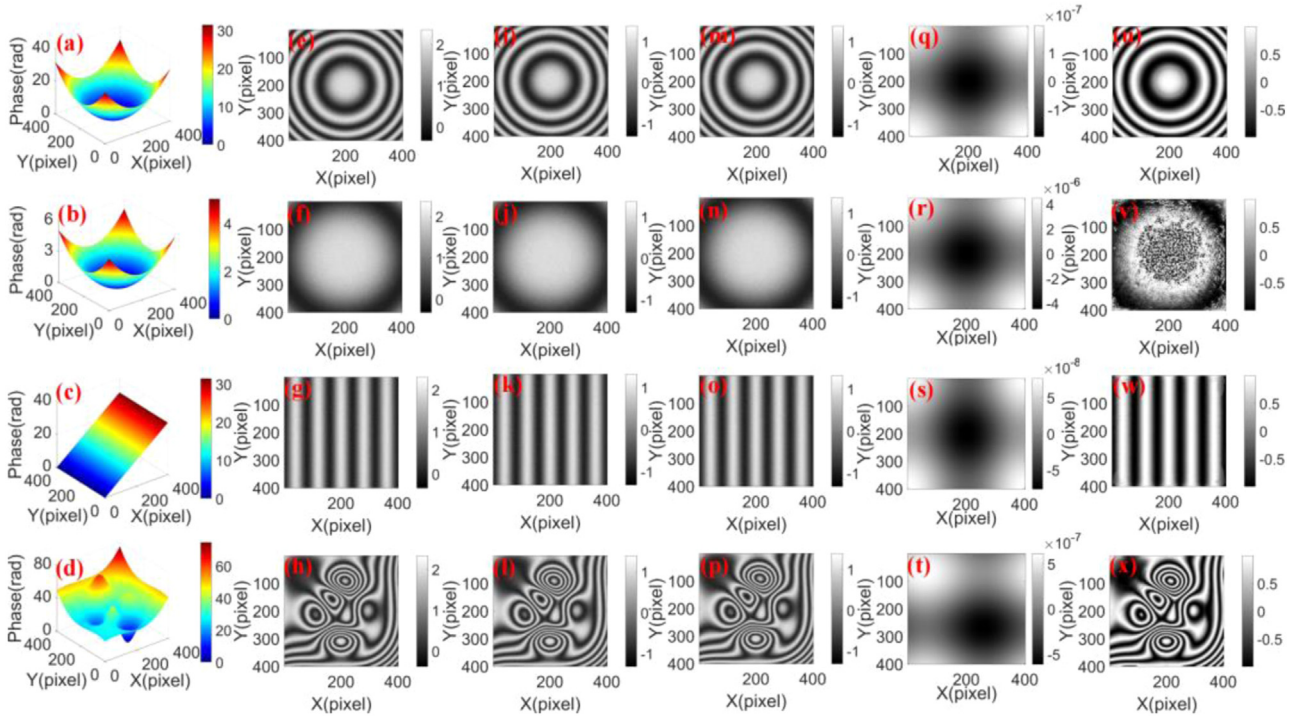

Fig. 1. Simulated phase distributions and phase-shifting interferograms. (a)-(b) Theoretical phase distributions corresponding to the circular fringes ((a) fringe number=5, (b) fringe number=0.8); (c)-(d) Theoretical phase distributions corresponding to the straight and complex fringes; (e)-(h) Corresponding interferograms related to Fig. 1(a)-1(d); (i)-(l) Interferograms after Gaussian high-pass filtering; (m)-(p) Interferograms after subtracting the mean intensity; (q)-(t) Difference maps between (i)-(l) and (m)-(p); (u)-(x) Interferograms after HHT.

$10(\frac{1}{5}x - x^3 - y^5)e^{-x^2-y^2} - \frac{1}{3}e^{-(x+1)^2-y^2}]$. In the practical situation, the background intensity and modulation amplitude will be non-uniform between different pixels and variational between different interferograms, therefore we set the background intensity and modulation amplitude as $a_i(x, y) = R_a \exp[-0.02(x^2 + y^2)]$and $b_i(x, y) = R_b \exp[-0.02(x^2 + y^2)]$, and $R_a$of two interferograms are respectively 1 and 0.95, R_b of two interferograms are respectively 0.95 and 0.9. In addition, 20 dB of noise is added to the phase-shifting interferograms with the size of 401×401, and the phase shift between two phase-shifting interferograms is 1 rad. The 1st interferograms corresponding to Fig. 1 (a)-1(d) are shown in Fig. 1 (e)-1(h). Fig. 1(e) and 1(f) are both circular fringes, but the fringe number is different, the fringe number is respectively 5 and 0.8. In addition, Fig. 1(g) and 1(h) show straight and complex fringes respectively. The interferograms after Gaussian high-pass filtering are shown in Fig. 1(i)-1(l). Moreover, we also subtract the mean intensity to remove the background, as displayed in Fig. 1(m)-1(p). To compare the two background removal methods, the difference maps of interferograms are shown in Fig. 1 (q)-(t). We can see that the two methods have similar accuracy, however, the mean intensity subtraction costs only 0.006 s, Gaussian high-pass filtering costs 0.127 s. Hence, we choose the mean intensity subtraction as a background removal method in the following. But the mean intensity subtraction can only remove the background, but not the noise, which will affect the accuracy of phase reconstruction. The interferograms after HHT are shown in Fig. 1(u)-1(x). From the processed interferograms, we can see that HHT can filter both background and noise. However, the filtering error will affect the accuracy of phase reconstruction, what's more, when there is less than one fringe number, the filtering error is considerably large, which will affect the subsequent phase reconstruction. Both noise and filtering error will affect the performance of TS-PSAs-BR, so it is worth studying which has more effect on the phase reconstruction.

10 TS-PSAs are performed to reconstruct the phase, and their acronyms are listed in Table 1. The phase error maps corresponding to different types of fringes are demonstrated in Figs. 2–5. It is clear

Table 1
Acronyms of algorithms.

Algorithm Name	Acronym
Two-step phase-shifting algorithms	TS-PSAs
TS-PSAs with background removal	TS-PSAs-BR
TS-PSAs with no background removal	TS-PSAs-NBR
TS-PSAs with background removal by Hilbert-Huang Transform	TS-PSAs-BR-H
TS-PSAs with background removal by mean intensity subtraction	TS-PSAs-BR-M
Gram-Schmidt orthonormalization method with Hilbert-Huang Transform	GS-H
Gram-Schmidt orthonormalization method with mean intensity subtraction	GS-M
Diamond diagonal vectors algorithm with Hilbert-Huang Transform	DDV-H
Diamond diagonal vectors algorithm with mean intensity subtraction	DDV-M
Extreme values of the interference algorithm with Hilbert-Huang Transform	EVI-H
Extreme values of the interference algorithm with mean intensity subtraction	EVI-M
Quotient of inner products algorithm with Hilbert-Huang Transform	QIP-H
Quotient of inner products algorithm with mean intensity subtraction	QIP-M
Coefficient of variation minimization method with Hilbert-Huang Transform	CVM-H
Coefficient of variation minimization method with mean intensity subtraction	CVM-M
Quartic polynomial equation solving algorithm with Hilbert-Huang Transform	QPE-H
Quartic polynomial equation solving algorithm with mean intensity subtraction	QPE-M
Gram-Schmidt orthonormalization and Lissajous ellipse fitting method	GS&LEF
Principal component analysis and Lissajous ellipse fitting method	PCA&LEF
Lissajous ellipse fitting and least-squares iterative algorithm	LEF&LSI
Euclidean matrix norm of sum and difference map and fast least-squares algorithm	EMNSD&FLSA

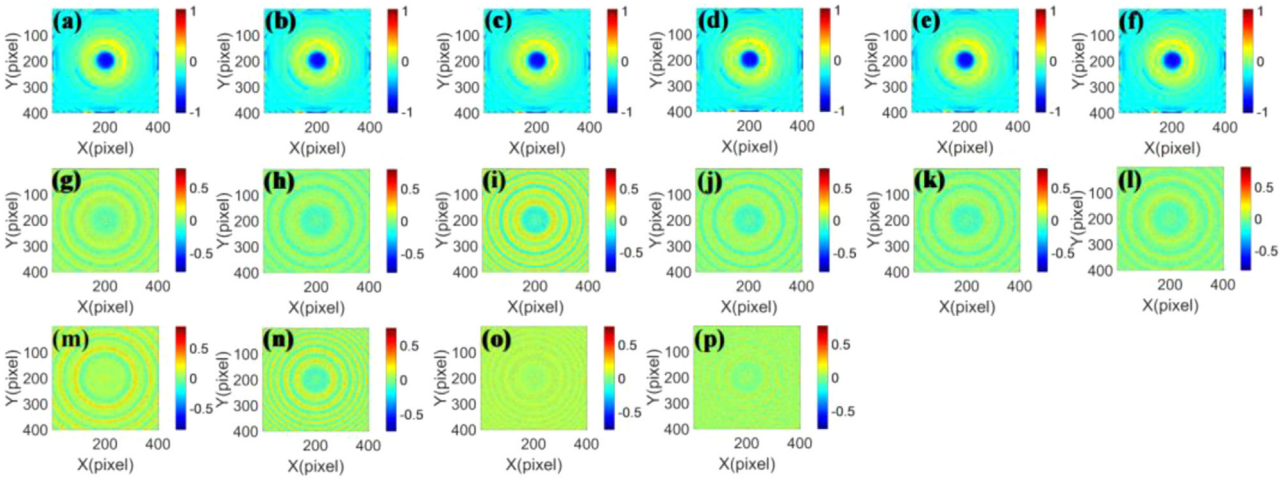

Fig. 2. Phase error maps corresponding to the circular fringes (fringe number=5). (a)-(f) Phase error maps after using GS-H, DDV-H, EVI-H, QIP-H, CVM-H, QPE-H; (g)-(l) Phase error maps after using GS-M, DDV-M, EVI-M, QIP-M, CVM-M, QPE-M; (m)-(p) Phase error maps after using GS&LEF, PCA&LEF, LEF&LSI and EMNSD&FLSA.

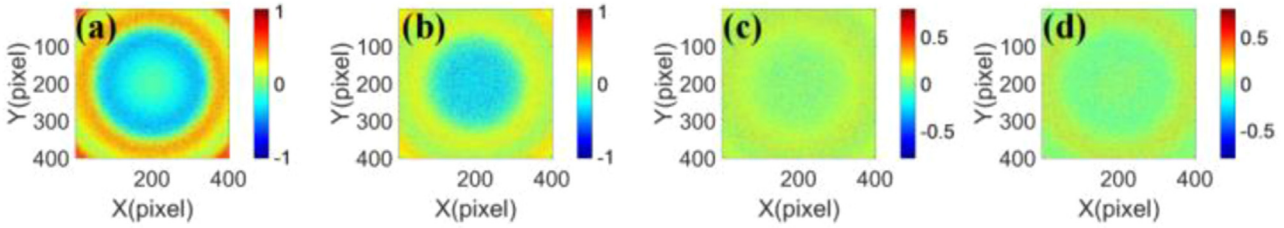

Fig. 3. Phase error maps corresponding to the circular fringes (fringe number=0.8). (a)-(d) Phase error maps after using GS&LEF, PCA&LEF, LEF&LSI and EMNSD&FLSA.

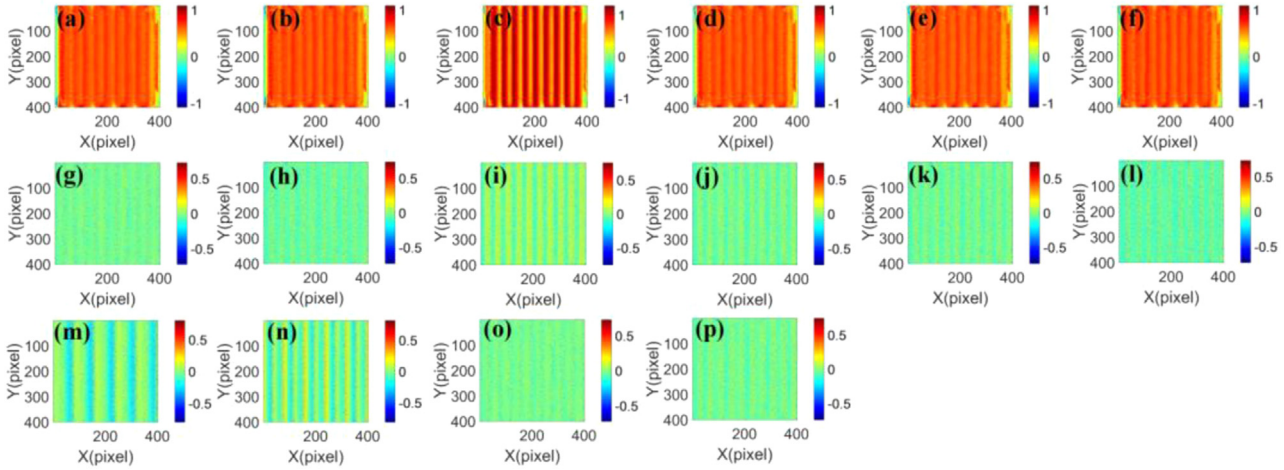

Fig. 4. Phase error maps corresponding to the straight fringes. (a)-(f) Phase error maps after using GS-H, DDV-H, EVI-H, QIP-H, CVM-H, QPE-H; (g)-(l) Phase error maps after using GS-M, DDV-M, EVI-M, QIP-M, CVM-M, QPE-M; (m)-(p) Phase error maps after using GS&LEF, PCA&LEF, LEF&LSI and EMNSD&FLSA.

that the accuracy of TS-PSAs-BR-M is higher than that of TS-PSAs-BR-H because HHT can introduce filtering error. When the fringe number of circular fringes is 0.8, TS-PSAs-BR don't work since HHT introduces a large filtering error, and the mean intensity subtraction requires the fringe number to be more than one. In addition, many TS-PSAs-BR can only work when the fringe number is more than one due to the approximation requirement. Nevertheless, TS-PSAs-NBR are effective for the situation with less than one fringe number because they don't require background removal, and there is no approximation in phase reconstruction.

In the following, the effect of noise on different TS-PSAs will be studied, with noise ranging from 20 dB to 50 dB. When the fringe number is 5, Fig. 6(a) shows the phase errors RMS of different TS-PSAs corresponding to the circular fringes with different levels of noise. The accuracy of TS-PSAs-BR-M is higher than that of TS-PSAs-BR-H for any level of noise, and the accuracy of TS-PSAs-NBR is higher than that of TS-PSAs-BR except that the noise is 20 dB. The phase errors RMS are similar for different TS-PSAs-BR-H with different levels of noise since the filtering error is the main error among all errors. With the same level of noise, the phase errors RMS of TS-PSAs-BR-M have little differ-

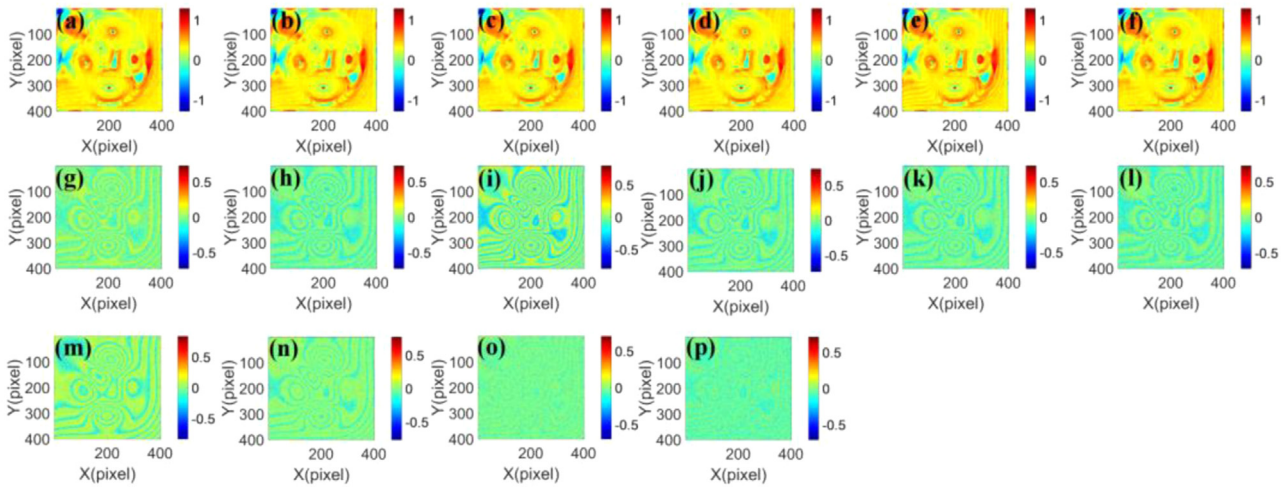

Fig. 5. Phase error maps corresponding to the complex fringes. (a)-(f) Phase error maps after using GS-H, DDV-H, EVI-H, QIP-H, CVM-H, QPE-H; (g)-(l) Phase error maps after using GS-M, DDV-M, EVI-M, QIP-M, CVM-M, QPE-M; (m)-(p) Phase error maps after using GS&LEF, PCA&LEF, LEF&LSI and EMNSD&FLSA.

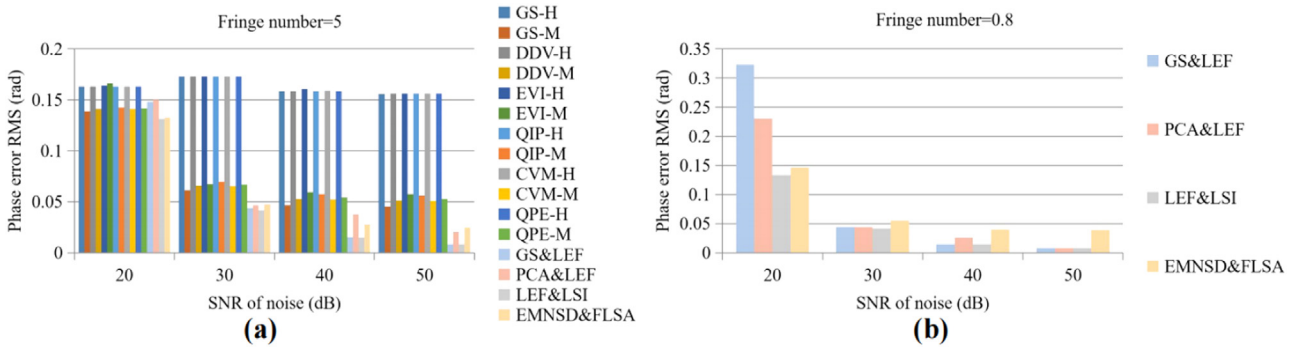

Fig. 6. Phase errors RMS of different TS-PSAs corresponding to the circular fringes with different levels of noise.

ence because noise as the main error also exists in the interferograms. In addition, the accuracy of TS-PSAs-BR-M and TS-PSAs-NBR increases with the decrease of noise. When the noise exceeds 30 dB, TS-PSAs-NBR are more accurate than TS-PSAs-BR since TS-PSAs-NBR don't perform background removal before phase reconstruction. However, when the noise is 20 dB, GS&LEF and PCA&LEF are less accurate than TS-PSAs-BR-M, and LEF&LSI and EMNSD&FLSA are more accurate than other TS-PSAs. LEF&LSI and EMNSD&FLSA are iterative PSAs, therefore more accurate phase can be obtained from noisy interferograms.

When the fringe number is 0.8, TS-PSAs-NBR also work. The phase errors RMS with different levels of noise are drawn in Fig. 6(b), and the phase errors RMS decrease with the decrease of noise. When the noise is 20 dB, the phase errors RMS of GS&LEF and PCA&LEF are relatively large since they obtain the phase without any filtering and iteration, the effect of noise is relatively large.

When the noise is 20 dB, the phase errors RMS of different TS-PSAs corresponding to the circular (fringe number=5), straight and complex fringes are displayed in Fig. 7(a). All TS-PSAs are suitable for different types of fringes. With regard to circular fringes, the phase errors RMS of different TS-PSAs have little difference. However, the phase error RMS of EVI-H is significantly larger than that of other TS-PSAs when the fringe is straight. And when the fringe is complex, the phase errors RMS of TS-PSAs-BR-H are much larger than those of other TS-PSAs. Hence, TS-PSAs-BR-H are more suitable for circular and straight fringes.

To evaluate the inherent error of TS-PSAs, we simulate different types of fringes with perfect background intensity and modulation amplitude. Moreover, there is no noise in the interferograms. Fig. 7(b) displays the results. For different types of fringes, TS-PSAs-NBR can obtain the accurate phase without any error. For all types of fringes, the phase errors RMS of TS-PSAs-BR-H are extremely large because of the filtering error. The phase errors RMS of TS-PSAs-BR-M for the straight fringes are close to zero. However, with regard to the circular and complex fringes, there are the phase errors for TS-PSAs-BR-M, and the phase errors RMS are similar. In other words, for straight fringes, the mean intensity subtraction can efficiently remove the background, but for circular and complex fringes, the error of mean intensity subtraction is relatively large. Furthermore, from Fig. 7, we can clearly see that EVI-H performs worse than any other TS-PSAs in the situation of straight fringes, so EVI-H is unsuitable for straight fringes.

To evaluate the effect of different phase shifts on different TS-PSAs and the valid phase shift range of TS-PSAs at different levels of noise, we simulate different phase shifts in the range of 0.1 rad to 3.1 rad, as shown in Figs. 8 and 9. For both 20 dB and 0 dB of noise, the phase errors RMS of TS-PSAs-BR-H are independent of the phase shift and PSA since the effect of filtering error is greater than that of different phase shifts and PSAs. When the noise is 20 dB, the curves of phase error RMS of GS-M, DDV-M, QIP-M, CVM-M, QPE-M, LEF&LSI, EMNSD&FLSA are relatively smooth, and the closer the phase shift is to $\pi/2$, the smaller the phase error RMS is. But the curves of EVI-M, GS&LEF and PCA&LEF are unsmooth. When there is no noise, the phase errors RMS are relatively stable with different phase shifts, the phase errors RMS increase only when the phase shift is close to 0 or π. Moreover, the curves of PCA&LEF and LEF&LSI are unsmooth even without noise.

There is an interesting phenomenon that, when the noise is 20 dB, the phase errors RMS of GS-M, DDV-M, QIP-M, CVM-M, QPE-M with the phase shift ranging from 0.8 rad to 2.4 rad are less than those of GS-H,

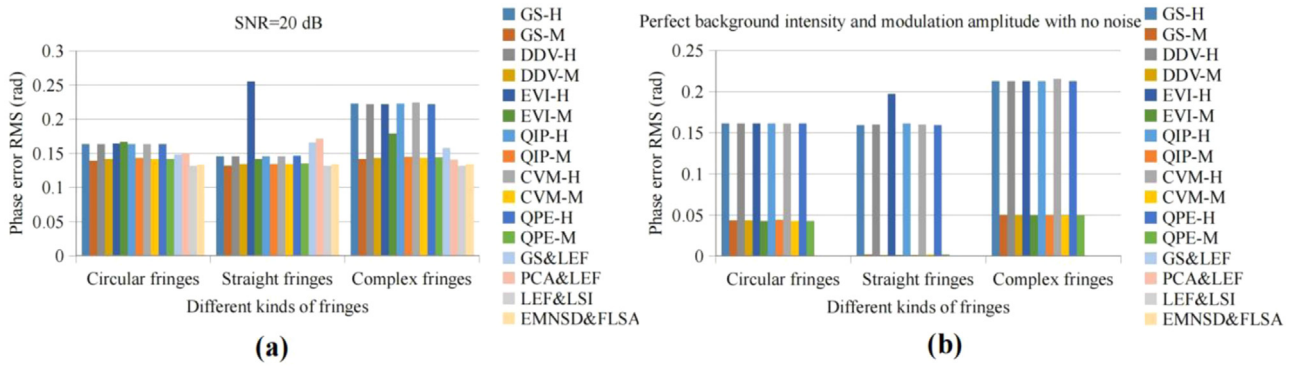

Fig. 7. Phase errors RMS of different TS-PSAs with different types of fringes.

DDV-H, QIP-H, CVM-M, QPE-H, for other phase shifts, the conclusion is opposite. The reason for the above phenomenon is that the noise has a greater effect on GS-M, DDV-M, QIP-M, CVM-M, QPE-M when the phase shift approaches 0 or π. Although EVI doesn't have the same conclusion, the curve trend is similar to that of other TS-PSAs-BR. When there is no noise, the phase errors RMS of GS-M, DDV-M, CVM-M, QPE-M are less than those of GS-H, DDV-H, CVM-H, QPE-H for any phase shift. And, QIP-M and EVI-M are more accurate than QIP-H and EVI-H except for individual phase shifts. The reason why different levels of noise lead to different conclusions is that mean intensity subtraction can't eliminate noise.

For TS-PSAs-NBR, when the noise is 20 dB, the phase errors RMS of LEF&LSI and EMNSD&FLSA are similar and less than those of GS&LEF and PCA&LEF because LEF&LSI and EMNSD&FLSA are iterative PSAs that can obtain more accurate phase from noisy interferograms. Nevertheless, when there is no noise in the interferograms, the phase errors RMS of PCA&LEF and EMNSD&FLSA are larger than those of GS&LEF and LEF&LSI, indicating that the effect of non-uniform and variational background intensity and modulation amplitude on PCA&LEF and EMNSD&FLSA is larger than that on GS&LEF and LEF&LSI. LEF&LSI performs better than other TS-PSAs-NBR for both 20 dB and 0 dB of noise.

Further, we discuss the valid phase shift range of different TS-PSAs. When the noise is 20 dB, the phase shift ranges of TS-PSAs-BR-H which are 2.4 rad are larger than those of TS-PSAs-BR-M and TS-PSAs-NBR since HHT filters most of the noise, then increases the valid phase shift range. For TS-PSAs-BR-M and TS-PSAs-NBR, the phase shift range of GS&LEF which is 1.9 rad is the least, and EMNSD&FLSA has the largest phase shift range which is 2.2 rad, other TS-PSAs have the same phase shift range which is 2.1 rad. When there is no noise, the phase shift ranges of GS-M, DDV-M, QIP-M, CVM-M and TS-PSAs-NBR which are 2.9 rad are larger than those of TS-PSAs-BR-H which are 2.6 rad since the filtering error affects the phase shift range, and the phase shift ranges of EVI-M and QPE-M are relatively small due to the algorithm itself. In addition, the valid phase shift ranges of all TS-PSAs for the interferograms with no noise are larger than those for the interferograms with 20 dB of noise.

To summarize, when the noise in the interferograms is large, it is best to choose the TS-PSAs-BR-H, LEF&LSI and EMNSD&FLSA with phase shifts close to $\pi/2$. Moreover, when there is less noise or no noise, TS-PSAs-BR-M and TS-PSAs-NBR with phase shifts away from 0 and π are more suitable.

Different fringe numbers are simulated to analyze the performance and effective fringe number range of different TS-PSAs. The fringe number range is set between 0.2 and 5. Note that 5 is not the maximum fringe number, most PSAs will work with more fringe number. We both simulate the situations with 20 dB and 0 dB of noise, Figs. 10 and 11 show the results. It can be seen that TS-PSAs-BR-M are more accurate than TS-PSAs-BR-H except GS in the situation of 20 dB of noise. When there is no noise, TS-PSAs-BR-H perform poorly for several fringe numbers because HHT may introduce relatively large error in some situations. When the noise is 20 dB, LEF&LSI and EMNSD&FLSA perform better and are more stable than other TS-PSAs. When there is no noise, GS&LEF, LEF&LSI and EMNSD&FLSA are relatively stable and perform better than other TS-PSAs, moreover, EMNSD&FLSA performs slightly worse than GS&LEF and LEF&LSI.

From Figs. 10(h) and 11(h), we can conclude that the effective fringe number range of TS-PSAs-BR is independent of noise. The effective fringe number range of TS-PSAs-BR-H is from 1.4 to 5.0, and the effective fringe number range of TS-PSAs-BR-M is from 1.2 to 5.0. The effective fringe number range of TS-PSAs-NBR is larger than that of TS-PSAs-BR because HHT introduces a larger error when the fringe number is less than one, and the mean intensity subtraction requires more than one fringe number. Moreover, some TS-PSAs-BR also require more than one fringe number due to the approximation. For TS-PSAs-NBR except EMNSD&FLSA, since no filtering is performed, the noise will affect the effective fringe number range. The effective fringe number range is from 0.2 to 5 in the situation of no noise, and it is from 0.6 to 5 in the situation of 20 dB of noise. When there is no noise, the effective fringe number range of EMNSD&FLSA is from 0.4 to 5.0, which is slightly smaller than that of other TS-PSAs-NBR, the possible reason is that sometimes the approximation of Eq. (42) could affect the accuracy of iteration.

In addition, when the noise is 20 dB, and there are more than 3 fringe number, the phase errors RMS of TS-PSAs-BR are more stable. When there is more than one fringe number, the phase errors RMS of LEF&LSI and EMNSD&FLSA are more stable. And the phase errors RMS of GS&LEF and PCA&LEF are unstable in the whole range of fringe number. When there is no noise, and the fringe number is larger than 2, TS-PSAs-BR-H performs stably, however, TS-PSAs-BR-M sometimes perform unstably. When the fringe number is larger than one, TS-PSAs-NBR except PCA&LEF perform stably. Overall, the effective fringe number range of TS-PSAs-NBR is larger than that of TS-PSAs-BR, and LEF&LSI outperforms other TS-PSAs in terms of different fringe numbers and effective fringe number range.

The efficiency of PSA is as important as its accuracy, hence we calculate the computational time of different TS-PSAs corresponding to the circular fringes, as displayed in Fig. 17 and Table 2. Except CVM-H and QPE-H, the computational time of TS-PSAs-BR-H is similar, because HHT takes the most time. And CVM-H and QPE-H cost more time since the phase shift search also costs lots of time. TS-PSAs-BR-M cost less time than TS-PSAs-BR-H because the mean intensity subtraction takes almost no time, and CVM-M and QPE-M spend the major time on searching the phase shift. LEF&LSI costs the most time for all TS-PSAs because of the process of LSI. Although EMNSD&FLSA is also an iterative algorithm, it takes very little time since only a limited number of pixels are selected to take part in the iterative process. In addition, GS&LEF and PCA&LEF

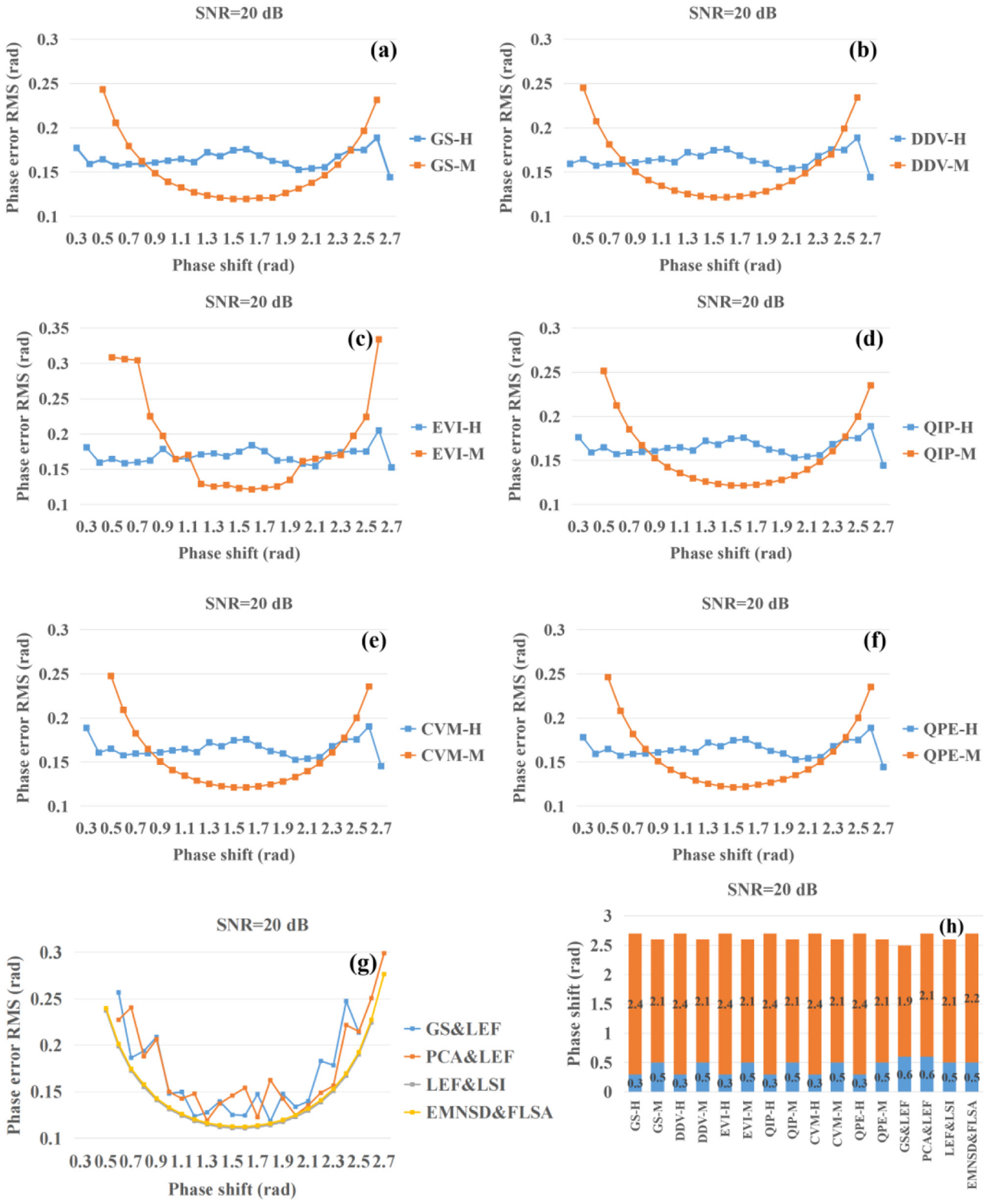

Fig. 8. (a)-(g) Phase errors RMS of different TS-PSAs corresponding to the circular fringes with different phase shifts and 20 dB of noise; (h) The valid phase shift range of different TS-PSAs with 20 dB of noise.

cost the similar amount of time because LEF takes up most of the time. As a whole, the computational time in descending order is: LEF&LSI, CVM-H and QPE-H, TS-PSAs-BR-H except CVM-H and QPE-H, CVM-M and QPE-M, GS&LEF and PCA&LEF, EMNSD&FLSA, and TS-PSAs-BR-M except CVM-M and QPE-M.

4. Comparisons of TS-PSAs in the experiments

Experimental data are also used to compare the performance of TS-PSAs. Three groups of experiments corresponding to the circular, straight and complex fringes are carried out respectively. Four phase-

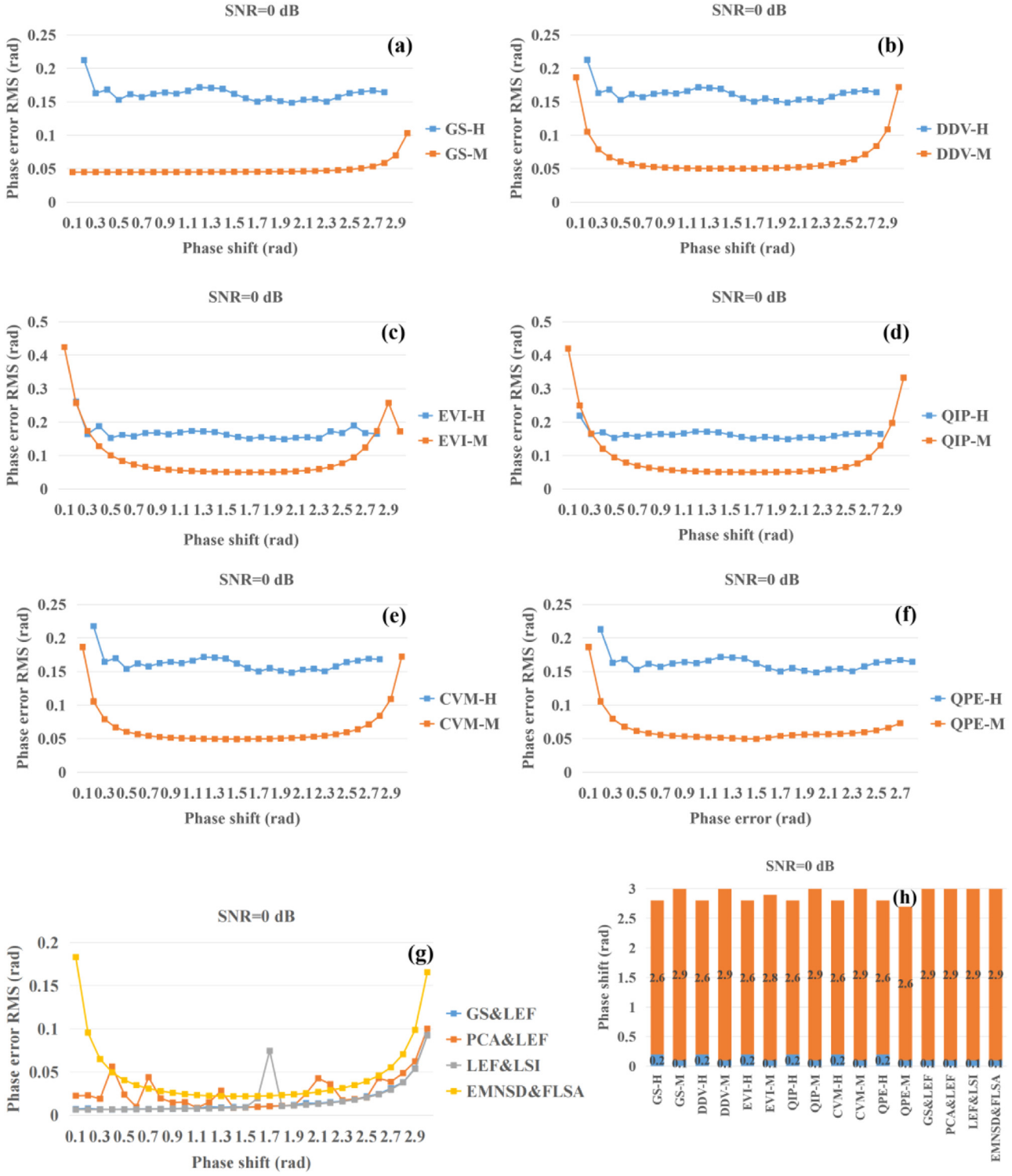

Fig. 9. (a)-(g) Phase errors RMS of different TS-PSAs corresponding to the circular fringes with different phase shifts and no noise; (h) The valid phase shift range of different TS-PSAs with no noise.

shifting interferograms with phase shifts of 0, $\pi/2$, π, and $3\pi/2$ for each experiment are captured by the snapshot phase-shifting interferometer. The phase shift error is relatively small because only a single image snapshotted is extracted by the polarization camera, then the accurate phase calculated by standard 4-step PSA can be used as the reference phase. Fig. 12(a)-12(f) shows the reference phase distributions and 1st phase-shifting interferograms corresponding to the circular, straight and complex fringes. Fig. 12(g)-12(l) displays the interferograms after HHT and mean intensity subtraction. The image quality of interferograms after HHT is significantly improved. However, the image quality of interferograms after mean intensity subtraction is the same as that of the original interferograms.

We use the first two phase-shifting interferograms for phase reconstruction, the phase error maps are plotted in Figs. 13-15, and the phase errors RMS of different TS-PSAs with different types of fringes are displayed in Fig. 16. Generally, the experimental conditions are more com-

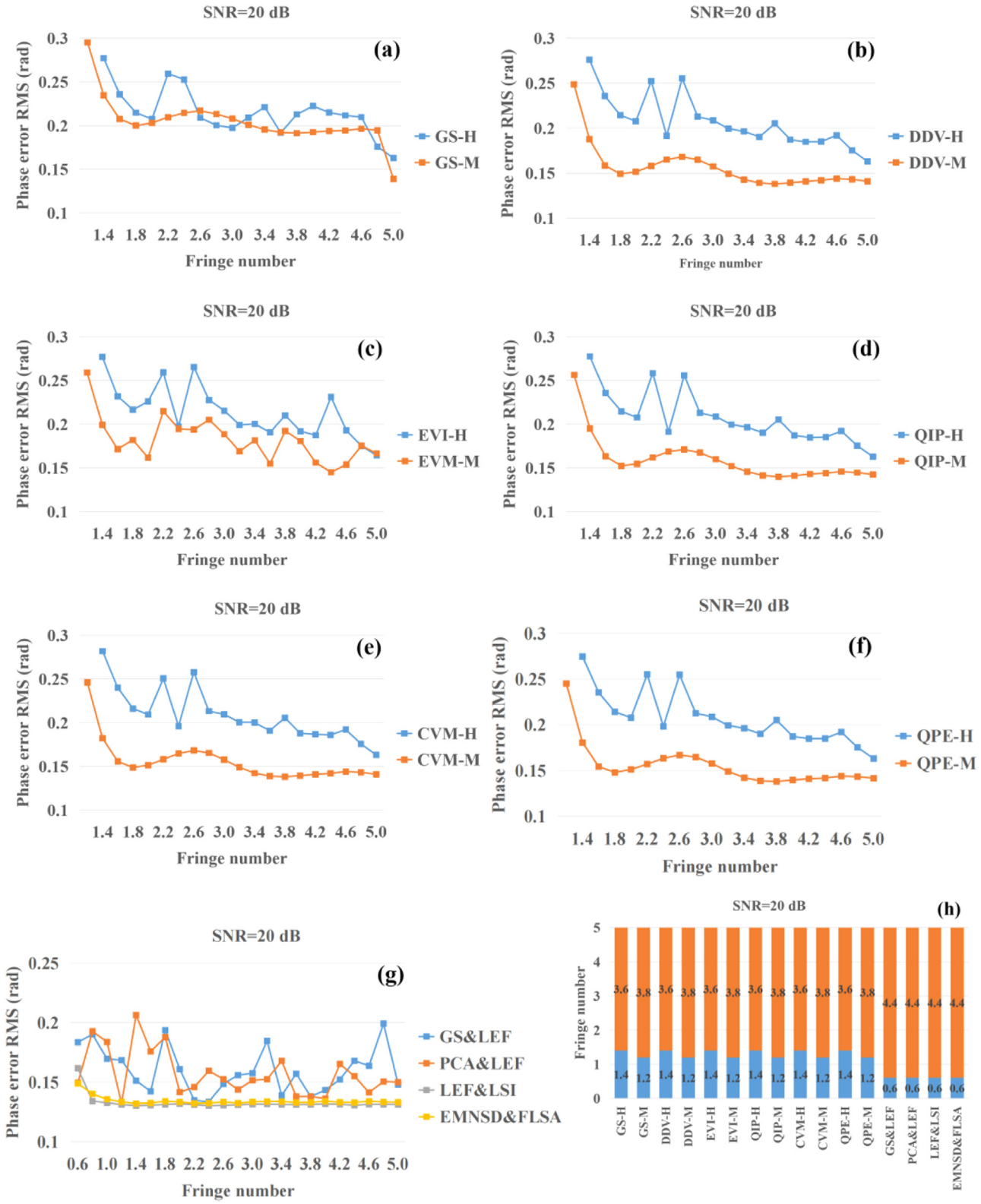

Fig. 10. (a)-(g) Phase errors RMS of different TS-PSAs corresponding to the circular fringes with different fringe numbers and 20 dB of noise; (h) The effective fringe number ranges of different TS-PSAs with 20 dB of noise.

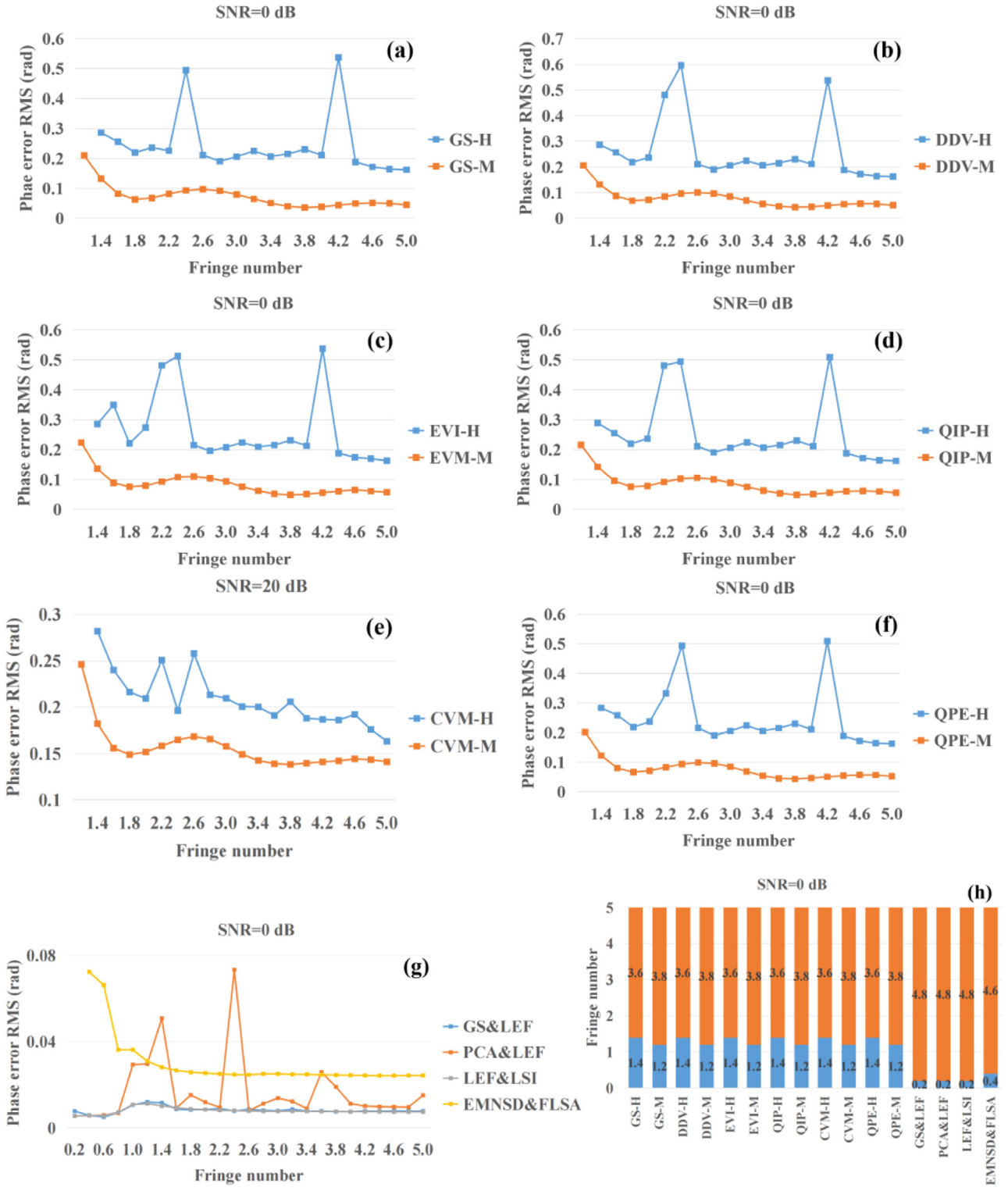

Fig. 11. (a)-(g) Phase errors RMS of different TS-PSAs corresponding to the circular fringes with different fringe numbers and no noise; (h) The effective fringe number ranges of different TS-PSAs with no noise.

plex than the simulated ones. Hence, some PSAs with strict requirements on the quality of the interferogram don't work in the experiments, for example, EVI-M doesn't work for circular and complex fringes in the experiments. But EVI-H is effective in any case because HHT can improve the quality of the interferogram. Because the fringe number is more than one for all types of fringes in the experiments, TS-PSAs except EVI-M work well.

By comparing different TS-PSAs in the experiments, we can get similar conclusions to the simulations. The phase errors RMS of TS-PSAs-BR-H are similar. The performance of TS-PSAs-BR-M is similar with regard to the circular and complex fringes. Nevertheless, when the fringes are straight, EVI-M and QPE-M perform worse than other TS-PSAs-BR-M. With regard to TS-PSAs-NBR, different types of fringes give different conclusions, TS-PSAs-NBR with circular fringes have similar accuracy.

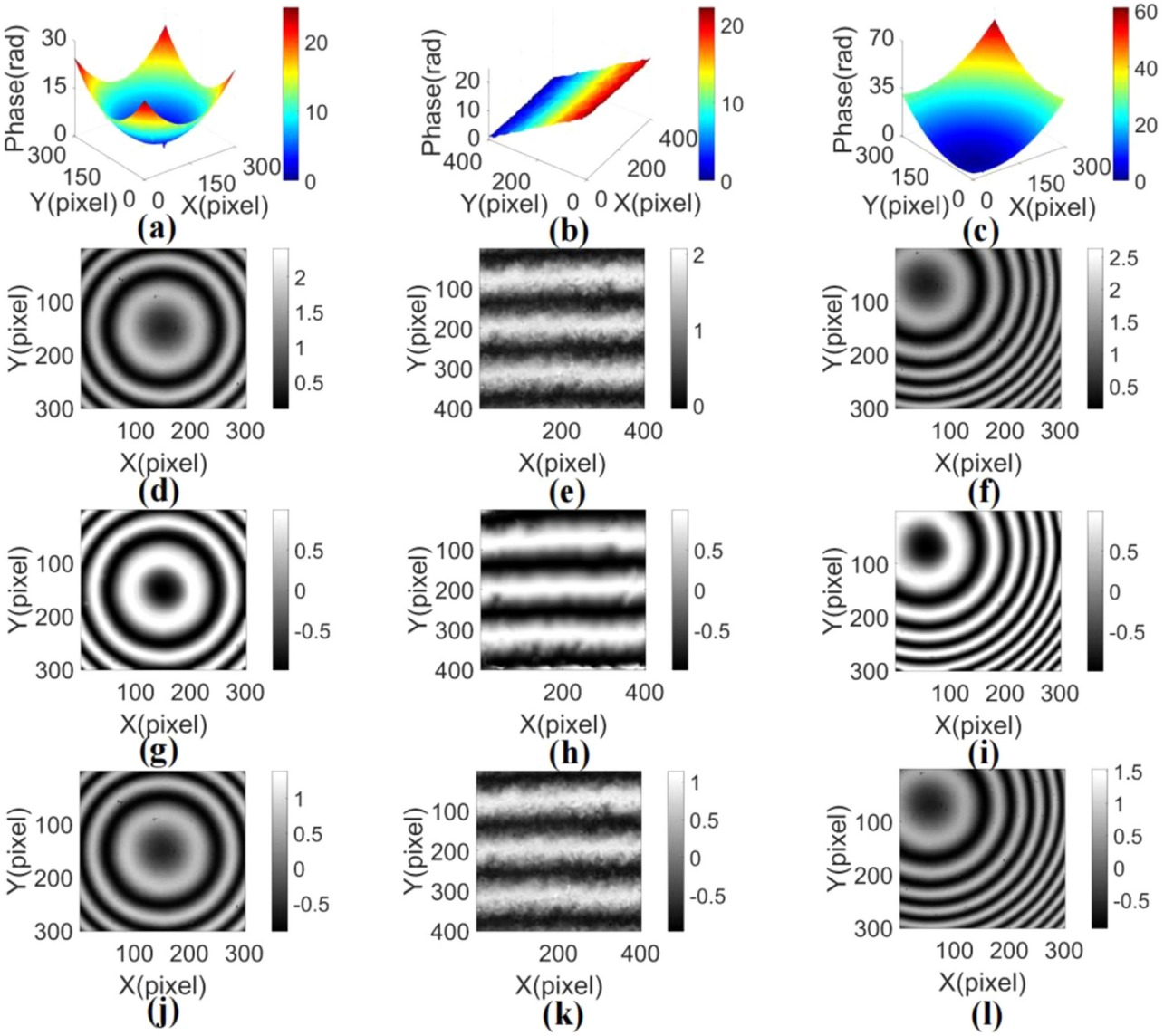

Fig. 12. Experimental phase distributions and phase-shifting interferograms. (a)-(c) Reference phase distributions corresponding to the circular, straight and complex fringes reconstructed by 4-step PSA; (d)-(f) Corresponding interferograms related to Fig. 12(a)-12(c); (g)-(i) Interferograms after HHT; (j)-(l) Interferograms after subtracting the mean of the interferogram.

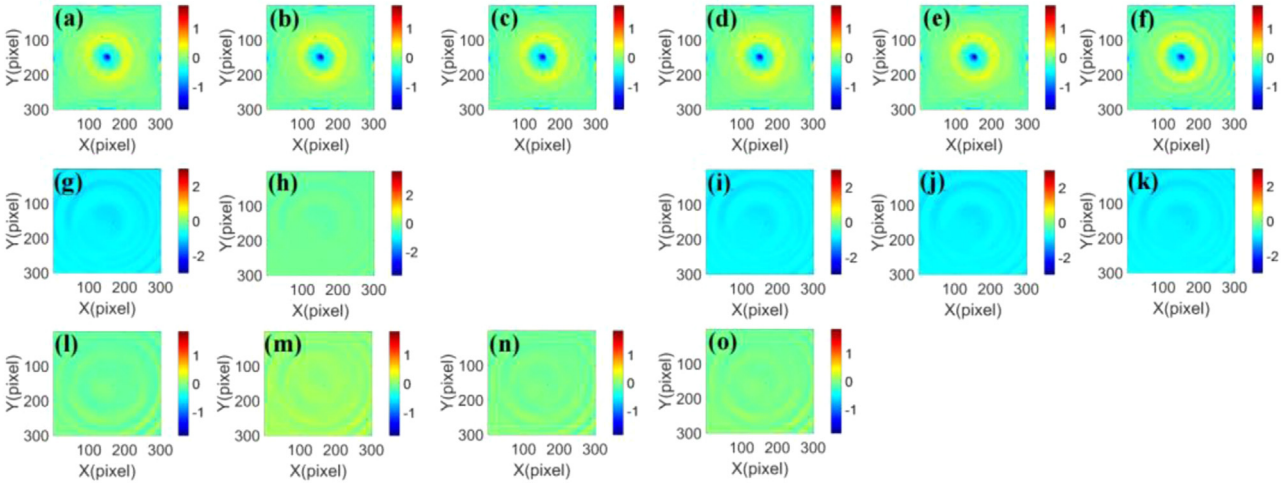

Fig. 13. Phase error maps corresponding to the circular fringes in the experiments. (a)-(f) Phase error maps of GS-H, DDV-H, EVI-H, QIP-H, CVM-H, QPE-H; (g)-(k) Phase error maps of GS-M, DDV-M, QIP-M, CVM-M, QPE-M; (l)-(o) Phase error maps of GS&LEF, PCA&LEF, LEF&LSI and EMNSD&FLSA.

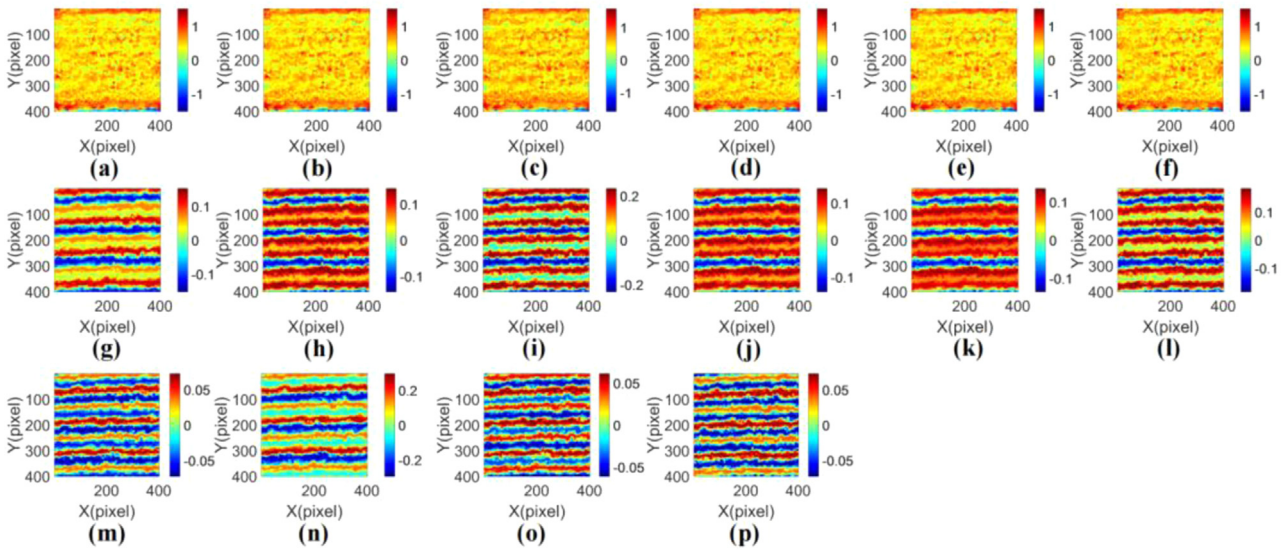

Fig. 14. Phase error maps corresponding to the straight fringes in the experiments. (a)-(f) Phase error maps of GS-H, DDV-H, EVI-H, QIP-H, CVM-H, QPE-H; (g)-(l) Phase error maps of GS-M, DDV-M, EVI-M, QIP-M, CVM-M, QPE-M; (m)-(p) Phase error maps of GS&LEF, PCA&LEF, LEF&LSI and EMNSD&FLSA.

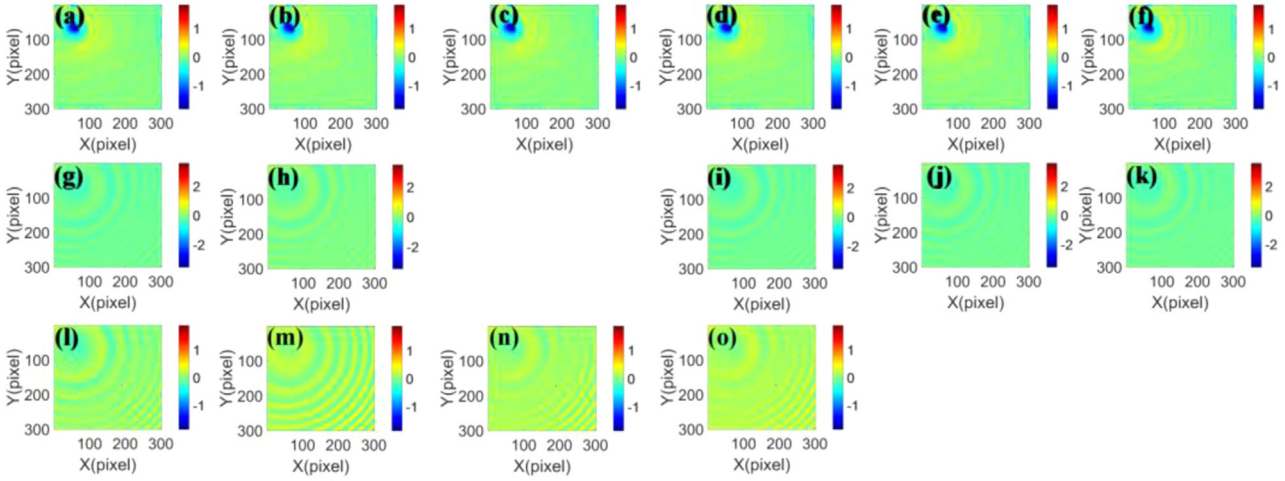

Fig. 15. Phase error maps corresponding to the complex fringes in the experiments. (a)-(f) Phase error maps of GS-H, DDV-H, EVI-H, QIP-H, CVM-H, QPE-H; (g)-(k) Phase error maps of GS-M, DDV-M, QIP-M, CVM-M, QPE-M; (l)-(o) Phase error maps of GS&LEF, PCA&LEF, LEF&LSI and EMNSD&FLSA.

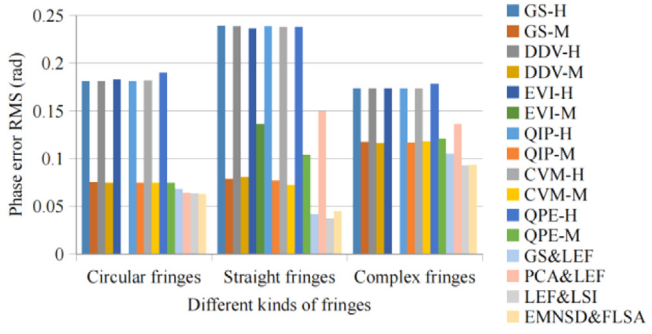

Fig. 16. Phase errors RMS of different TS-PSAs with different types of fringes in the experiments.

For straight and complex fringes, TS-PSAs-NBR except PCA&LEF also have similar accuracy, and PCA&LEF performs worse. In addition, TS-PSAs-NBR except PCA&LEF are superior to TS-PSAs-BR in the situation of straight and complex fringes.

We also evaluate the computational time of different TS-PSAs corresponding to the circular fringes in the experiment, as shown in Fig. 17 and Table 2. The computational time of the simulations and experiments is not similar due to the different number of pixels. In terms of computational time, similar results are obtained from simulations and experiments.

5. Conclusions

We demonstrated the performance comparison of well-reputed TS-PSAs with unknown phase shift. We compared different TS-PSAs with different types of fringes, different levels of noise, different phase shifts, different fringe numbers and computational time in the simulations. To verify the correctness of the simulations, three different types of fringes were also used to compare different TS-PSAs in the experiments. We divided TS-PSAs into two types, one is TS-PSAs-BR, the other one is TS-PSAs-NBR. Moreover, TS-PSAs-BR can also be divided into two types, one is TS-PSAs-BR-H, and the other one is TS-PSAs-BR-M. Both HHT and mean intensity subtraction aim to remove the background, but HHT can also filter the noise.

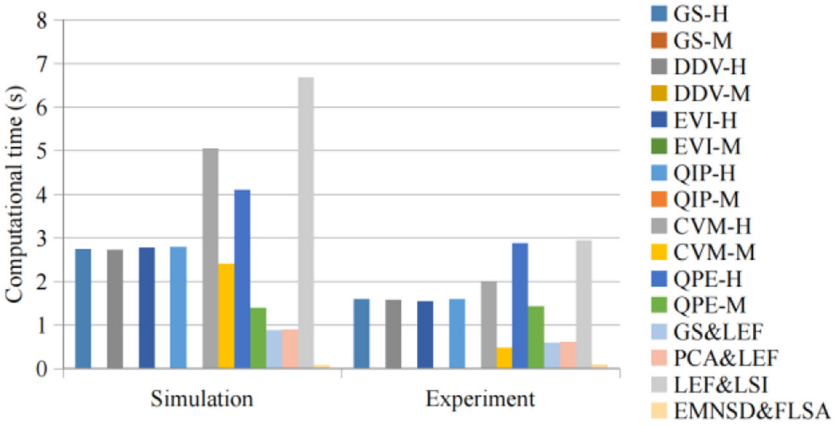

Fig. 17. Computational time of different TS-PSAs corresponding to the circular fringes in the simulations and experiments (s).

Table 2
Computational time (s).

	Simulation (401 × 401 pixels)	Experiment (301 × 301 pixels)
GS-H	2.733	1.605
GS-M	0.011	0.006
DDV-H	2.718	1.576
DDV-M	0.009	0.005
EVI-H	2.771	1.555
EVI-M	0.011	–
QIP-H	2.781	1.605
QIP-M	0.007	0.005
CVM-H	5.041	2.018
CVM-M	2.407	0.479
QPE-H	4.107	2.877
QPE-M	1.394	1.427
GS-LEF	0.889	0.599
PCA-LEF	0.899	0.616
LEF-LSI	6.676	2.936
EMNSD&FLSA	0.085	0.099

Table 3 presents the results of the comparison, and we rate the grade of performance as good, medium and poor. Note that these TS-PSAs are all well-reputed algorithms, and the grade is only set for comparing different TS-PSAs.

In summary, TS-PSAs-H have the largest valid phase shift range, and they are almost insensitive to phase shifts. However, they are less accurate than other TS-PSAs with different levels of noise and different types of fringes, and they have the smallest fringe number range. They also performed worse in the experiments, and they cost relatively more time due to filtering. TS-PSAs-BR-M except EVI-M have medium performance in terms of different levels of noise, different types of fringes, different phase shifts and different fringe numbers, and they performed the same in the experiments. Their valid phase shift range is less than TS-PSAs-BR-H, and their effective fringe number range is less than TS-PSAs-NBR, but they cost the least time. EVI-M is an algorithm that requires high-quality interferograms, so sometimes it doesn't work or performs poorly. TS-PSAs-NBR have the largest fringe number range, and GS&LEF performs moderately in terms of different levels of noise, experiments and computational time, but it performs poorly in terms of different types of fringes, and its valid phase shift range with 20 dB of noise is minimum. The performance of PCA&LEF is similar to that of GS&LEF, but the valid phase shift range of PCA&LEF is larger than that of GS&LEF, and in the experiments, PCA&LEF didn't perform as well as GS&LEF since PCA&LEF is more susceptible to complex environment. LEF&LEI and EMNSD&FLSA perform similarly, and they do best in different levels of noise, different types of noise, different fringe numbers and experiments. When there is 20 dB of noise, their valid phase shift range is less than TS-PSAs-BR-H. However, there is a huge difference in their computational time, EMNSD&FLSA costs very little time, LEF&LSI takes the most time of any TS-PSA because LEF&LSI uses all pixels to take part in the calculation. If we choose a limited number of pixels to take part in the iterative process of LEF&LSI, their computational time can be reduced.

Through the above analysis, if we rank TS-PSAs by performance, the grades are divided into five levels. Grade 1 is the best, and Grade 5 is the worst, the results are listed in Table 4. Although these TS-PSAs

Table 3
Comparison of performance with regard to TS-PSAs (G, M and P are the grades of performance corresponding to good, medium and poor).

	Different noise			Different types of fringes			Different phase shifts			Different fringe numbers			Experiments			Computational time		
	G	M	P	G	M	P	G	M	P	G	M	P	G	M	P	G	M	P
GS-H			△			△	√					△			△		○	
GS-M		○			○			○			○			○		√		
DDV-H			△			△	√					△			△		○	
DDV-M		○			○			○			○			○		√		
EVI-H			△			△	√					△			△		○	
EVI-M			△			△			△		○				△	√		
QIP-H			△			△	√					△			△		○	
QIP-M		○			○			○			○			○		√		
CVM-H			△			△	√					△			△			△
CVM-M		○			○			○			○			○			○	
QPE-H			△			△	√					△			△			△
QPE-M		○			○			○			○				△		○	
GS-LEF		○				△			△	√				○			○	
PCA-LEF		○				△		○		√					△		○	
LEF-LSI	√			√				○		√			√					△
EMNSD&FLSA	√			√				○		√			√			√		

Table 4
The grades of all TS-PSAs.

Grade	1	2	3	4	5
TS-PSAs	EMNSD&FLSA	LEF&LSI	GS-M DDV-M QIP-M	CVM-M QPE-M GS-LEF PCA-LEF	GS-H DDV-H EVI-H QIP-H CVM-H QPE-H EVI-M

are classified into different levels, they are suitable for different situations. TS-PSAs-BR-H are suitable for situations with lots of noise, large fringe number and relatively random phase shift. TS-PSAs-BR-M are appropriate for situations with large fringe number, moderate phase shift and little noise, and GS-M, DDV-M, EVI-M and QIP-M are also suitable for in-situ measurement. GS&LEF and PCA&LEF are suitable for situations with little noise, moderate phase shift and relatively arbitrary fringe number. LEF&LSI and EMNSD&FLSA are appropriate for situations with lots of noise, moderate phase shift and relatively arbitrary fringe number. In addition, EMNSD&FLSA is also suitable for in-situ measurement.

We can see that different background removal methods have different effects on TS-PSAs-BR, these TS-PSAs themselves are excellent. However, HHT introduces a large filtering error, and it takes lots of time. Moreover, the mean intensity subtraction can't remove the noise, therefore TS-PSAs-BR-M are susceptible to noise. TS-PSAs-NBR don't need to remove the background, hence they are not affected by the background removal methods. However, GS&LEF and PCA&LEF perform very ordinarily since the noise will affect them, and there is no iteration to reduce the effect of noise. LEF&LSI and EMNSD&FLSA are two iterative TS-PSAs. General iterative PSAs have higher accuracy but low efficiency, LEF&LSI really is, but EMNSD&FLSA can achieve both high accuracy and high efficiency.

In the future, we should aim at improving background removal methods to remove the background with high accuracy and high efficiency for TS-PSAs-BR, saving iterative time and ensuring iterative accuracy for iterative TS-PSAs-NBR, and the enlargement of valid phase shift range is also essential for TS-PSAs-NBR.

Funding

This work was supported by the National Natural Science Foundation of China (grant number 61905039) and Science and Technology Research Project of Jilin Provincial Education Department (grant number JJKH20220093KJ).

Declaration of Competing Interest

The authors declare the following financial interests/personal relationships which may be considered as potential competing interests: None

CRediT authorship contribution statement

Yu Zhang: Conceptualization, Methodology, Formal analysis, Funding acquisition. **Bao Liu:** Investigation, Data curation, Software, Funding acquisition. **Rongguang Liang:** Writing – review & editing.

Data Availability

Data will be made available on request.

Supplementary materials

Supplementary material associated with this article can be found, in the online version, at doi:10.1016/j.optlaseng.2022.107327.

References

[1] Malacara D. Optical shop testing. New Jersey: John Wiley & Sons Inc; 2007. p. 1–274.
[2] Bruning JH, Herriott DR, Gallagher JE, Rosenfeld DP, White AD, Brangaccio DJ. Digital wavefront measuring interferometer for testing optical surfaces and lenses. Appl Opt 1974;13(11):2693–703. doi:10.1364/AO.13.002693.
[3] Tian C, Liu S. Two-frame phase-shifting interferometry for testing optical surfaces. Opt Express 2016;24(16):18695–708. doi:10.1364/OE.24.018695.
[4] Wu R, Feng Z, Zheng Z, Liang R, Benítez P, Minano JC, Duerr F. Design of freeform illumination optics. Laser Photonics Rev 2018:1700310. doi:10.1002/lpor.201700310.
[5] Shen F, Yang L, Hu G, Ding Z, She J, Zhang Y, Wu R. Freeform and precise irradiance tailoring in arbitrarily oriented planes. Opt Express 2021;29(26):42844–54. doi:10.1364/OE.445593.
[6] Malacara D. Optical shop testing. New Jersey: John Wiley & Sons Inc; 2007. p. 547–666.
[7] Servin M, Marroquin JL, Cuevas FJ. Fringe-follower regularized phase tracker for demodulation of closed-fringe interferograms. J Opt Soc Am A 2001;18(3):689–95. doi:10.1364/JOSAA.18.000689.
[8] Liu D, Yang Y, Wang L, Zhuo Y. Real time diagnosis of transient pulse laser with high repetition by radial shearing interferometer. Appl Opt 2007;46(34):8305–14. doi:10.1364/AO.46.008305.
[9] Garbusi E, Pruss C, Osten W. Single frame interferogram evaluation. Appl Opt 2008;47(12):2046–52. doi:10.1364/AO.47.002046.
[10] Tian C, Yang Y, Wei T, Ling T, Zhuo Y. Demodulation of a single-image interferogram using a Zernike-polynomial-based phase-fitting technique with a differential evolution algorithm. Opt Lett 2011;36(12):2318–20. doi:10.1364/OL.36.002318.
[11] Yuan S, Hu Y, Hao Q, Zhang S. High-accuracy phase demodulation method compatible to closed fringes in a single-frame interferogram based on deep learning. Opt Express 2021;29(2):2538–54. doi:10.1364/OE.413385.
[12] Sun Y, Bian Y, Shen H, Zhu R. High-accuracy simultaneous phase extraction and unwrapping method for single interferogram based on convolutional neural network. Opt Laser Eng 2022;151:106941. doi:10.1016/j.optlaseng.2021.106941.
[13] Wang Z. Advanced iterative algorithm for phase extraction of randomly phase-shifted interferograms. Opt Lett 2004;29(14):1671–3. doi:10.1364/OL.29.001671.
[14] Vargas J, Quiroga J, Belenguer T. Phase-shifting interferometry based on principal component analysis. Opt Lett 2011;36(8):1326–8. doi:10.1364/OL.36.001326.
[15] Vargas J, Quiroga J, Belenguer T. Analysis of the principle component algorithm in phase-shifting interferometry. Opt Lett 2011;36(12):2215–17. doi:10.1364/OL.36.002215.
[16] Xu J, Jin W, Chai L, Xu Q. Phase extraction from randomly phase-shifted interferograms by combining principal component analysis and least squares method. Opt Express 2011;19(21):20483–92. doi:10.1364/OE.19.020483.
[17] Yatabe K, Ishikawa K, Oikawa Y. Hyper ellipse fitting in subspace method for phase-shifting interferometry: practical implementation with automatic pixel selection. Opt Express 2017;25(23):29401–16. doi:10.1364/OE.25.029401.
[18] Deng J, Wang K, Wu D, Lv X, Li C, Hao J, Qin J, Chen W. Advanced principal component analysis method for phase reconstruction. Opt Express 2015;23(9):12222–31. doi:10.1364/OE.23.012222.
[19] Wang H, Luo C, Zhong L, Ma S, Lu X. Phase retrieval approach based on the normalized difference maps induced by three interferograms with unknown phase shifts. Opt Express 2014;22(5):5147–54. doi:10.1364/OE.22.005147.
[20] Meneses-Fabian C, Lara-Cortes FA. Phase retrieval by Euclidean distance in self-calibrating generalized phase-shifting interferometry of three steps. Opt Express 2015;23(10):13589–604. doi:10.1364/OE.23.013589.
[21] Xu Y, Wang Y, Ji Y, Han H, Jin W. Three-frame generalized phase-shifting interferometry by a Euclidean matrix norm algorithm. Opt Laser Eng 2016;84:89–95. doi:10.1016/j.optlaseng.2016.04.011.
[22] Escobar MA, Estrada JC, Vargas J. Phase-shifting VU factorization for interferometry. Opt Lasers Eng 2020;124:105797. doi:10.1016/j.optlaseng.2019.105797.
[23] Meneses-Fabian C. Self-calibrating generalized phase-shifting interferometry of three phase-steps based on geometric concept of volume enclosed by a surface. J Opt-UK 2016;18:125703. doi:10.1088/2040-8978/18/12/125703.
[24] Gomez-Conde JC, Meneses-Fabian C. Real-time phase step measurement using the volume enclosed by a surface algorithm in self-calibrating phase-shifting interferometry. Measurement 2020;153:107412. doi:10.1016/j.measurement.2019.107412.
[25] Gomez-Conde JC, Meneses-Fabian C. Real-time measurements of phase steps out-of-range (0, 2π) by a dynamic self-calibrating generalized phase-shifting algorithm. Opt Laser Eng 2021;140:106543. doi:10.1016/j.optlaseng.2021.106543.

[26] Kreis TM, Jueptner WPO. Fourier transform evaluation of interference patterns: demodulation and sign ambiguity. Proc SPIE 1992;1553:263273. doi:10.1117/12.135312.
[27] Vargas J, Quiroga JA, Belenguer T, Servín M, Estrada JC. Two-step self-tuning phase-shifting interferometry. Opt Express 2011;19(2):638–48. doi:10.1364/OE.19.000638.
[28] Vargas J, Quiroga JA, Sorzano COS, Estrada JC, Carazo JM. Two-step interferometry by a regularized optical flow algorithm. Opt Lett 2011;36(17):3485–7. doi:10.1364/OL.36.003485.
[29] Vargas J, Quiroga JA, Sorzano COS, Estrada JC, Carazo JM. Two-step demodulation based on the Gram-Schmidt orthonormalization method. Opt Lett 2012;37(3):443–5. doi:10.1364/OL.37.000443.
[30] Deng J, Wang H, Zhang F, Zhang D, Zhong L, Lu X. Two-step phase demodulation algorithm based on the extreme value of interference. Opt Lett 2012;37(22):4669–71. doi:10.1364/ol.37.004669.
[31] Ma J, Wang Z, Pan T. Two-dimensional continuous wavelet transform algorithm for phase extraction of two-step arbitrarily phase-shifted interferograms. Opt Lasers Eng 2014;55:205–11. doi:10.1016/j.optlaseng.2013.11.009.
[32] Trusiak M, Patorski K. Two-shot fringe pattern phase-amplitude demodulation using Gram-schmidt orthonormalization with HHT. Opt Express 2015;23(4):4672–90. doi:10.1364/OE.23.004672.
[33] Wielgus M, Sunderland Z, Patorski K. Two-frame tilt-shift error estimation and phase demodulation algorithm. Opt Lett 2015;40:3460–3. doi:10.1364/OL.40.003460.
[34] Luo C, Zhong L, Sun P, Wang H, Tian J, Lu X. Two-step demodulation algorithm based on the orthogonality of diamond diagonal vectors. Appl Phys B 2015;119:387–91. doi:10.1007/s00340-015-6087-z.
[35] Niu W, Zhong L, Sun P, Zhang W, Lu X. Two-step phase retrieval algorithm based on the quotient of inner products of phase-shifting interferograms. J Opt 2015;17:085703. doi:10.1088/2040-8978/17/8/085703.
[36] Rivera M, Dalmau O, Gonzalez A, Hernandez-Lopez F. Two-step fringe pattern analysis with a Gabor filter bank. Opt Lasers Eng 2016;85:29–37. doi:10.1016/j.optlaseng.2016.04.014.
[37] Xu X, Shou J, Lu X, Yin Z, Tian J, Li D, Zhong L. Independent component analysis based two-step phase retrieval algorithm. J Opt-UK 2016;18:105701. doi:10.1088/2040-8978/18/10/105701.
[38] Tian C, Liu S. Two-frame phase-shifting interferometry for testing optical surfaces. Opt Express 2016;24:18695–708. doi:10.1364/OE.24.018695.
[39] Tian C, Liu S. Demodulation of two-shot fringe patterns with random phase shifts by use of orthogonal polynomials and global optimization. Opt Express 2016;24:3202–15. doi:10.1364/OE.24.003202.
[40] Dalmau O, Rivera M, Gonzalez A. Phase shift estimation in interferograms with unknown phase step. Opt Commun 2016;372:37–43. doi:10.1016/j.optcom.2016.03.063.
[41] Tian C, Liu S. Phase retrieval in two-shot phase-shifting interferometry based on phase shift estimation in a local mask. Opt Express 2017;25:21673–83. doi:10.1364/OE.25.021673.
[42] Saide D, Trusiak M, Patorski K. Evaluation of adaptively enhanced two-shot fringe pattern phase and amplitude demodulation methods. Appl Opt 2017;56:5489–500. doi:10.1364/AO.56.005489.
[43] Kulkarni R, Rastogi P. Two-step phase demodulation algorithm based on quadratic phase parameter estimation using state space analysis. Opt Laser Eng 2018;110:41–6. doi:10.1016/j.optlaseng.2018.05.012.
[44] Cheng Z, Liu D. Fast and accurate wavefront reconstruction in two-frame phase-shifting interferometry with unknown phase step. Opt Lett 2018;43(13):3033–6. doi:10.1364/ol.43.003033.
[45] Cheng Z, Liu D, Zhang L. Random two-frame phase-shifting interferometry via minimization of coefficient of variation. Appl Phys Lett 2019;115:121107. doi:10.1063/1.5118296.
[46] Zhang H, Zhao H, Zhao J, Zhao Z, Fan C. Two-shot fringe pattern phase demodulation using the extreme value of interference with Hilbert-Huang per-filtering. Proc SPIE 2019;11056:1105646 Optical Measurement Systems for Industrial Inspection XI. doi:10.1117/12.2525960.
[47] Farrell CT, Player MA. Phase step measurement and variable step algorithms in phase-shifting interferometry. Meas Sci Technol 1992;3:953–8. doi:10.1088/0957-0233/3/10/003.
[48] Zhang Y, Tian X, Liang R. Two-step random phase retrieval approach based on Gram-Schmidt orthonormalization and Lissajous ellipse fitting method. Opt Express 2019;27(3):2575–88. doi:10.1364/OE.27.002575.
[49] Zhang Y, Tian X, Liang R. Accurate and fast two-step phase shifting algorithm based on principle component analysis and Lissajous ellipse fitting with random phase shift and no pre-filtering. Opt Express 2019;27(14):20047–63. doi:10.1364/OE.27.020047.
[50] Zhang Y. Random phase retrieval approach using Euclidean matrix norm of sum and difference map and fast least-squares algorithm. Opt Commun 2020;460:125174. doi:10.1016/j.optcom.2019.125174.
[51] Zhang Y, Tian X, Liang R. Random two-step phase shifting interferometry based on Lissajous ellipse fitting and least squares technologies. Opt Express 2018;26(12):15059–72. doi:10.1364/OE.26.015059.
[52] Estrada JC, Flores VH, Vargas J. A two steps phase-shifting demodulation method using the VU factorization. Opt Laser Eng 2021;147:106730. doi:10.1016/j.optlaseng.2021.106730.
[53] Muravsky LI, Kmet AB, Voronyak TI. Retrieving the relief of a low-roughness surface using a two-step interferometric method with blind phase shift of a reference wave. Opt Laser Eng 2012;50:1508–16. doi:10.1016/j.optlaseng.2012.06.011.
[54] Trusiak M, Patorski K, Wielgus M. Adaptive enhancement of optical fringe patterns by selective reconstruction using fabemd algorithm and hilbert spiral transform. Opt Express 2012;20(21):23463–79. doi:10.1364/OE.20.023463.
[55] Trusiak M, Patorski K, Wielgus M. Advanced processing of optical fringe patterns by automated selective reconstruction and enhanced fast empirical mode decomposition. Opt Laser Eng 2014;52:230–40. doi:10.1016/j.optlaseng.2013.06.003.
[56] Quiroga JA, Gómez-Pedrero JA, García-Botella Á. Algorithm for fringe pattern normalization. Opt Commun 2001;197(1-3):43–51. doi:10.1016/S0030-4018(01)01440-7.
[57] Quiroga JA, Servin M. Isotropic n-dimensional fringe pattern normalization. Opt Commun 2003;224(4-6):221–7. doi:10.1016/j.optcom.2003.07.014.